UPPSALA
UNIVERSITET

*Digital Comprehensive Summaries of Uppsala Dissertations from the Faculty of Science and Technology* 897

# New Materials for Spintronics

## *Electronic structure and magnetism*

RONNY KNUT



ACTA
UNIVERSITATIS
UPSALIENSIS
UPPSALA
2012

ISSN 1651-6214
ISBN 978-91-554-8275-6
urn:nbn:se:uu:diva-167415

Dissertation presented at Uppsala University to be publicly examined in Polhemsalen, Ångström Laboratory, Lägerhyddsvägen 1, Uppsala. Friday, March 16, 2012 at 10:15 for the degree of Doctor of Philosophy. The examination will be conducted in English.

**Abstract**
Knut, R. 2012. New Materials for Spintronics: Electronic structure and magnetism. Acta Universitatis Upsaliensis. *Digital Comprehensive Summaries of Uppsala Dissertations from the Faculty of Science and Technology* 897. 66 pp. Uppsala. ISBN 978-91-554-8275-6.

Materials exhibiting new functionalities due to interdependent electric (e.g. conductivity) and magnetic properties are potentially interesting for spintronics applications. We have investigated electronic and magnetic properties by means of x-ray spectroscopies and SQUID magnetometry in several magnetic materials, often in the form of thin films, which have shown promising properties for applications.

One of the main subjects has been studies of inter-diffusion between layers in multilayer structures, which is an important factor for spin-dependent transport and magnetic properties. These studies have been performed by high kinetic (HIKE) photoemission spectroscopy where high photon energies increase the bulk sensitivity in comparison to soft x-ray photoemission spectroscopy. Cu/Ni multilayers were studied mainly as a model system and revealed a diffusion process that was dependent on layer thicknesses and capping materials. CoFeB/MgO/CoFeB, which is used as a magnetic field sensor in hard drives, has recently been shown to exhibit a perpendicular magnetic anisotropy (PMA) switchable by electric fields. We have studied both the interface quality and magnetic properties of thin CoFeB layers exhibiting PMA. Layered structures of full Heusler alloys $Co_2MnGe$/$Rh_2CuSn$ have been proposed as a promising candidate for current-perpendicular-to-plane giant magneto-resistance sensors. Using HIKE,we have shown that diffusion of atoms, mainly Mn, occurs at temperatures lower than what is used in device fabrication, which likely contributes to the limited magneto-resistance values obtained.

Lately, a large body of research has been performed on semiconductors doped with transition metal elements with the hope to find a ferromagnetic semiconductor at room temperature, a foundation for new devices combining spin and charge in their functionality. We have investigated Co and Fe doping in ZnO for different concentrations of the dopants and different annealing temperatures. The Co and Fe atoms are shown to forms clusters for which antiferromagnetic interactions are dominating.

*Keywords:* Spintronics, X-ray photoemission, XPS, XMCD, XAS, magnetic semiconductors, HIKE, HAXPES, multilayer, monte carlo, magnetism

*Ronny Knut, Uppsala University, Department of Physics and Astronomy, Molecular and Condensed Matter Physics, 516, SE-751 20 Uppsala, Sweden.*



ISSN 1651-6214
ISBN 978-91-554-8275-6
urn:nbn:se:uu:diva-167415 (http://urn.kb.se/resolve?urn=urn:nbn:se:uu:diva-167415)

*To my friends and family*

# List of papers

This thesis is based on the following papers, which are referred to in the text by their Roman numerals.

I **Magnetic and electronic characterization of highly Co-doped ZnO: An annealing study at the solubility limit**
R. Knut, J. M. Wikberg, K. Lashgari, G. Westin, V. A. Coleman, P. Svedlindh and O. Karis, *PRB 82, 094438 (2010)*

II **Electronic structure and chemical and magnetic interactions in ZnO doped with Co and Al: Experiments and ab initio density-functional calculations**
D. Iusan, R. Knut, B. Sanyal, O. Karis, O. Eriksson V. A. Coleman, G. Westin, J. M. Wikberg and P. Svedlindh, *Phys. Rev. B 78, 8 (2008)*

III **Annealing effects on structural and magnetic properties of Co implanted ZnO single crystals**
J. M. Wikberg, R. Knut, A. Audren, M. Ottosson, M. K. Linnarsson, O. Karis, A. Hallen and P. Svedlindh, *J. Appl. Phys, 109, 083918 (2011)*

IV **Photoinduced reduction of surface states in the visible light sensitized photocatalyst Fe doped ZnO**
R. Knut, U. Kvist, P. Palmgren, P. Pal, P. Svedlindh, A. Pohl and O. Karis, *in manuscript*

V **Monte Carlo simulation as a sensitive characterization tool for exchange interactions and magnetic ion distributions**
R. Knut, U. Kvist, A. Pohl, O. Karis, B. Sanyal and P. Svedlindh, *in manuscript*

VI **Magnetocrystalline anisotropy and uniaxiality of MnAs/GaAs(100) films**
J. M. Wikberg, R. Knut, S. Bhandary, I. Di Marco, M. Ottosson, J. Sadowski, B. Sanyal, P. Palmgren, C. W. Tai, O. Eriksson, O. Karis and P. Svedlindh, *Phys. Rev. B 83, 024417 (2011)*

VII **XMCD study of PMA in CFB/MgO**
R. Knut, P. Warnicke, A. Sahoo, J. Persson, T. N. Anh Nguyen, S. M. Mohseni, T. Q. Le, D.D. Sarma, J. Åkerman, D. Arena and O. Karis, *in manuscript*

VIII **Interface characterization of $Co_2MnGe/Rh_2CuSn$ Heusler multilayers**
R, Knut, P. Svedlindh, K. Gunnarsson, O. Mryasov, P. Warnicke, D. Arena, M. Björk, D.D. Sarma, A. Sahoo, S. Mukherjee, S. Granroth, M. Gorgoi and O. Karis, *in manuscript*

IX **Investigation of interface properties of Ni/Cu multilayers by high kinetic energy photoelectron spectroscopy**
S. Granroth, R. Knut, M. Marcellini, G. Andersson, S. Svensson, O. Karis, M. Gorgoi, F. Scäfers, W. Braun, W. Eberhardt, W. Olovsson, E. Holmstrom and N. Martensson, *PRB 80, 094104 (2009)*

X **Understanding interface properties from high kinetic energy photoelectron spectroscopy and first principles theory**
S. Granroth, W. Olovsson, E. Holmstrom, R. Knut, M.Gorgoi, S. Svensson and O. Karis, *J. Electron. Spectrosc. Relat. Phenom. 183, 80 (2011)*

XI **Exploring the accessible frequency range of x-ray detected and phase-resolved ferromagnetic resonance**
P. Warnicke, R. Knut, E. Wahlström, O. Karis and D. A. Arena, *in manuscript*

XII **Inhomogeneity in Co doped ZnO diluted magnetic semiconductors**
B. Sanyal, R. Knut, O. Grånäs, D. M. Iusan, O. Karis, and O. Eriksson, *J. Appl. Phys. 103, 07D131 (2008)*

XIII **Ordering in diluted magnetic semiconductors: A magnetic percolation phenomenon**
O. Eriksson, R. Knut, D. M. Iusan, and B. Sanyal, *J. Appl. Phys. 101, 09H114 (2007)*

XIV **Electronic structure of Co doped ZnO: Theory and experiment**
B. Sanyal, O. Grånäs, R. Knut, V. A. Coleman, P. Thunström, D. M. Iusan, O. Karis, O. Eriksson, and G. Westin, *J. Appl. Phys. 103, 07D130 (2008)*

*The following are papers to which I have contributed but are not included in the thesis.*

**Atomic-scale chemical fluctuation in LaSrVMoO6, a proposed half-metallic antiferromagnet**
S. Jana, V. Singh, S. D. Kaushik, C. Meneghini, P. Pal, R. Knut, O. Karis, I. Dasgupta, V. Siruguri and S. Ray, *Phys. Rev. B 82, 180407 (2010)*

**Defect formation in graphene nanosheets by acid treatment: An x-ray absorption spectroscopy and density functional theory study**
V. A. Coleman, R. Knut, O. Karis, H. Grennberg, U. Jansson, R. Quinlan, B. C. Holloway, B. Sanyal and O. Eriksson, *J. Phys. D 41, 062001 (2008)*

# Comments on my own participation

My main contribution has been related to spectroscopic measurements at various synchrotron facilities. Though working at large scale facilities is always a teamwork due to the work patterns involved I have been in charge or directly involved in all synchrotron experiments presented in my thesis. For the papers where I am first author I have had the main responsibility of analyzing the data and writing the paper, otherwise my involvement is fairly represented by my position in the author list. For the purely theoretical work, my contribution has been through conducing Monte Carlo simulations where my involvement in DFT calculations has been through discussions. My main projects from the start of my PhD concerned wide-gap oxides doped with magnetic ions. In most of this work I was driving a substantial part of experimental work and paper writing. For the Monte Carlo analysis of the Fe-doped ZnO, I designed the model, performed the calculations and wrote the first version of the paper. Also the spectroscopic paper on the same material is largely realized by me. For the Co doped ZnO the situation is very similar and any deviation is reflected in my position in the author list. Regarding the work on the Heusler alloy multilayers I have been coordinating most the activities and taken essentially all spectroscopic data. I also wrote the first version of the paper presented in this thesis. All the work presented in the thesis is related to magnetic materials which has required a lot of SQUID magnetic measurements, my contribution to this part has been through discussion and to some extent analyzing but the experiments were performed by others.

# Contents

# 1. Svensk sammanfattning

## 1.1 Spinntronik

För 60 år sedan var elektronik främst förknippat med överföring av energi där ström användes för att ge ljus, värme och kraft till elektriska motorer. Idag är elektronik främst kopplat till informationshantering, då nästan alla elektriska maskiner innehåller kretsar som tar emot information och bearbetar den. Den revolution som har skett bygger på en elektrisk komponent, transistorn, som sedan gav integrerade kretsar där miljontals komponenter får plats på centimeterstora ytor.

Ända sedan den första datorn tillverkades har det funnits behov av att göra komponenterna mindre och datorerna snabbare. En känd förutsägelse om datorns kapacitet, är att den fördubblas vart annat år, den så kallade Moores lag. De komponenter som idag tillverkas har en tjocklek som inte är långt ifrån en miljondel av tjockleken på ett hårstrå och storleken börjar närma sig en gräns då det blir fysikaliskt omöjligt att göra komponenterna mindre. Detta faktum för fram forskning som man hoppas ska leda till helt nya typer av elektroniska komponenter, som kan ersätta eller öka kapaciteten i dagen kiselbaserade halvledarteknologi. Molekylbaserade transistorer, grafen (ett monolager av kolatomer) och det som denna avhandling fokuseras på, spinntronik är några av de forskningsområden där man söker nya material för informationshantering.

Dagens elektronik baseras på den elektriska laddning som elektroner har, utöver denna laddning så har elektronen även ett magnetisk moment som kallas för spinn. Spinntronik utnyttjar både elektronens laddning och spin, komponenter som baseras på spinntronik har funnits i nästan alla hårddiskar ända sedan slutet av 90-talet. Det vi talar om är läshuvudet, en sensor som känner av magnetiseringen av hårddisken och bygger på en Nobelprisbelönad (Albert Fert och Peter Grunberg 2007) princip som kallas för "giant magnetoresistance".

Skillnaden mellan elektronens laddning och spinn är att laddningen alltid är negativ, medan spinnet kan skifta mellan två tillstånd (två riktningar), vilket gör spinnet svårare att kontrollera. När en elektron färdas från ett material till ett annat, sker det lätt en oönskad förändring av spinnriktningen. Vi undersöker bland annat hur gränsytan mellan två olika material, som kan utnyttjas i spinnelektronikkomponenter, ser ut. Om gränsytan inte är skarp och materialen har blandats så ökar sannolikheten för oönskade förändringar i spinnladdningen.

En stor del av avhandlingen fokuserar på magnetiskt dopade halvledare, främst zinkoxid dopad med Co. I vanliga halvledare finns det begränsade möjlighet att kontrollera elektronens spinn, vilket skulle vara en mycket attraktiv egenskap då det skulle tillföra nya möjligheter till den redan väletablerade halvledarteknologin. Genom att dopa halvledare med magnetiska material så hoppas man kunna uppnå denna kontroll, vilket har visat sig vara mycket svårt att genomföra. Vi har undersökt magnetiskt dopade halvledar material både teoretiskt och experimentellt för olika variationer på tillverkning, uppvärming och dopningsmängd och därigenom försökt få en förståelse för vad som krävs av materialet för att tillverka en välfungerande magnetisk halvledare.

## 1.2 Synkrotronljus

Vi utnyttjar röntgenljus från synkrotroner för att karakterisera de material som presenteras i denna avhandling. En synkrotron består grovt förenklat, av en ringformad vakuumkammare , ofta hundratals meter i omkrets. Genom att få elektroner att färdas i nära ljusets hastighet inuti ringen, så avges röntgenljus.

Till skillnad mot andra röntgenljuskällor, som vi t.ex. använder för medicinsk röntgen på sjukhus, så har vi en möjlighet att variera energi och polarisation hos synkrotronljuset. Detta gör det möjligt att utföra en mängd olika experiment vid synkrotronljusanläggningar, där ofta hundratals användare från många olika naturvetenskapliga områden utnyttjar anläggningen. I mitt arbete har jag framförallt använt mig av röntgenabsorptions- och röntgenfotoemissionsspektroskopi samt magnetisk cirkulär dikroism med röntgenstrålning. Dessa experiment ger oss en god förståelse av elektronstrukturen hos atomerna i materialet och även information om magnetiska egenskaper som inte kan fås med andra metoder. I vissa fall använder vi röntgenljus med särskilt hög energi för att se djupare in i materialet (HIKE), eftersom flera av de metoder jag annars har använt är relativt ytkänsliga.

# 2. Introduction

People have been intrigued by magnetism for many centuries, at least until it became an everyday phenomenon to use small magnets for decoration on refrigerators. Magnetism was known before electricity and static electricity obtained by rubbing rods of amber with cat's fur was thought to be due to magnetism, since it attracted light objects like feathers. One of the earliest uses of magnetism is in compasses where the Earth's magnetic field aligns the magnetic moment of a magnet to point towards the Earth's magnetic poles. Without this magnetic field it would be nearly impossible for life to exist on our planet. It protects us from a huge amount of radiation from the sun, guiding the radiation to the poles where it sometimes shows up as northern or southern lights. For an extended enlightening overview in the history of magnetism I refer the interested reader to e.g. the book by P. Mohn [54].

In my youth, at the end of 80's, computers were scarce and friends who had a C-64 (a very modern personal computer in hose days) usually had a large set of magnetic tapes which contained the computer games. Not many years after, in the beginning and in the middle of the 90's, many of them, including me, had either an Amiga or Atari and now all the games were collected on floppy disks. Hard drives existed but were considered a luxury. However this changed fast and in the end of that decade the PC with built-in hard drives were common in most households in Sweden. All the different types of data storage mentioned above, have in common that magnetic domain contains the information and the constantly increasing need for storage capacity leads to new technology.

The research conducted in this thesis is not only focused on magnetic materials but without strong electromagnets the experiments described here could not have been conducted. Just like for the television (the old cathode ray tube type, more common at the scrapyard today than in the living room due to LED flat screens) and the microwave oven, we use magnets in our research for deflecting electrons in vacuum and thereby producing the x-rays used for studying electronic properties of materials.

All the above mentioned utilities are connected to static properties of magnets but with the discovery of giant magnetoresistance (GMR) it became clear that the dynamics between the electrons magnetic and electric properties could offer much more intriguing and versatile applications.

# 3. Spintronics

In traditional semiconductor electronics, it is only the charge of the electrons which is utilized. In spintronics, short for "spin electronics", also the spin of the charge carriers is used, by adding the property of the spin to conventional charge based electronics. The main goal in spintronic applications is to control, manipulate and measure the spin of an electric current. A well known review is the work by Wolf et al. [82]. In the presentation here I focus on the specific areas relevant to my work.

Today there are commercial spintronic devices which are widely used. In 1988, giant magnetoresistance (GMR) [64] was discovered which is considered to be the beginning of spintronics. In 1997 the success of this discovery became evident when the news of read heads for magnetic hard drives using GMR was announced by IBM. GMR is an effect observed in thin film structures with alternating ferromagnetic and nonmagnetic layers, often called spin valves, giving a high resistance if the magnetizations in the ferromagnetic layers are oppositely aligned and low resistance if they are aligned, see Fig. 3.1. The performance of GMR devices has now been surpassed by tunneling mag-

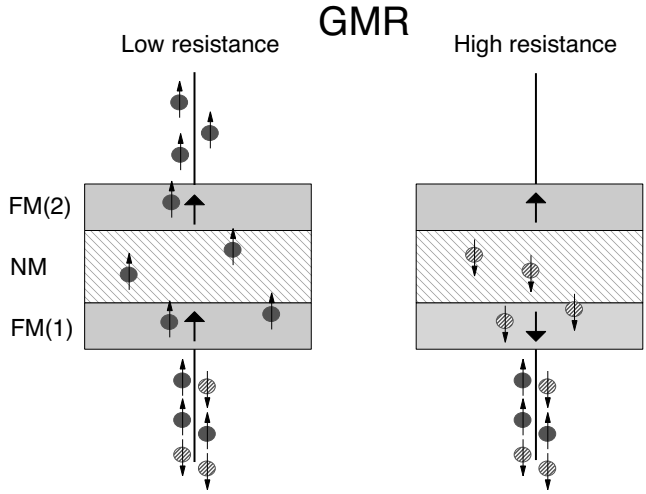


*Figure 3.1.* A simplified illustration of GMR. A non-spin polarized current enters the GMR structure but only one of the spin conduction bands (CB) are available in ferromagnet (FM) 1. (left) For low resistance the same spin CB is available in ferromagnet 2. (right) For high resistance there is no available CB in FM 2 for spins from FM 1.

netoresistance (TMR). It uses a similar device structure but with an insulating

non-magnetic layer, utilizing spin polarized tunnel currents. Both of these devices are mainly used as magnetic field detectors but similar principles are used in magnetic random access memories (MRAM) [44].

Even though the memory cells in an MRAM are too large for it to be a strong competitor to e.g. flash-memories, it exist as a commercial product. The large size is due to the writing process which uses magnetic fields created by electric currents. This method is not only energy consuming but it is also difficult to constrain the field in a small memory cell. An alternative way of writing is through spin transfer torque, which is still in the development stage [44]. Recent advances for thin CoFeB layers have shown the possibility for fast switching with small currents in memory cells [87].

Maintaing the performance of TMR devices while shrinking the sensor size for higher storage densities usually requires a reduction of the insulating layer thickness. This is already down at 1 nm, so further reduction is difficult. Therefore, it has been suggested that GMR could again become a competitor if the current-perpendicular-to-plane (CPP) geometry, which is illustrated in Fig. 3.1, can be developed. Large MR values have recently been demonstrated in this geometry using Co based Heusler alloys [68].

Heusler alloys are of special interest in the search for new spintronic materials since some of them exhibit a half-metallic character. This means that only one of the spin channels is available for the conduction electrons giving a 100% spin polarized current. The importance of such a material was demonstrated by Julliére [39] for the TMR effect

$$TMR = \frac{2P_1P_2}{1-P_1P_2}, \tag{3.1}$$

where $P_1$ and $P_2$ are the spin polarizations of the two ferromagnets in a TMR structure. For a 100% spin polarization the TMR becomes infinitely large.

Research concerning both CoFeB in TMR like structures and Heusler alloys for CPP-GMR structures are presented in the summary of papers section.

## 3.1 Dilute magnetic semiconductors

The possibility of integrating magnetic properties of electrons with semiconductor technology has gained much attention. Trying to accomplish this has turned out to be very difficult and one of the main problems is to inject a spin polarized current into semiconductors [82]. A ferromagnetic metal can in principle be used as a source of spin polarized carriers but when these carriers are injected into a semiconductor, the spin polarization more or less vanishes. The effectiveness of the spin injection is diminished by the conductivity mismatch between metals and semiconductors [70, 65]. A different solution would be a semiconductor which is a source of spin polarization by itself.

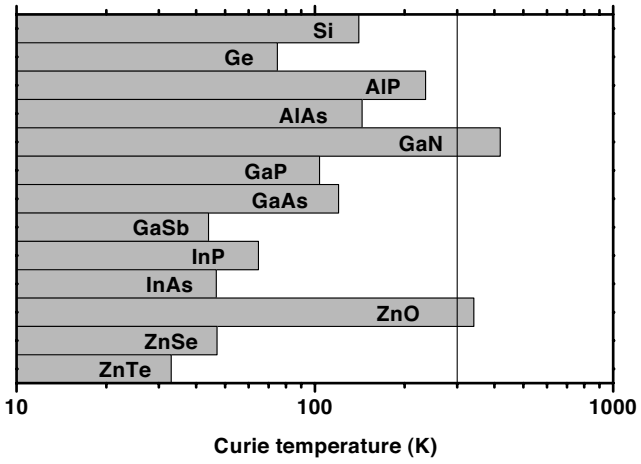


*Figure 3.2.* Predictions of Curie temperatures in 5% Mn doped semiconductors with $3.5 \cdot 10^{20}$ holes/cm$^3$. After Dietl et al. [20].

Dilute magnetic semiconductors (DMS) are materials where magnetic elements are doped into a semiconducting host, giving rise to both magnetic and semiconducting properties simultaneously. Semiconductors such as Eu- and Mn chalcogenides [32] are magnetic but are difficult to incorporate into the existing Si and GaAs based electronics. Furthermore, they are difficult to grow and have low Curie temperatures with a small prospect for improvement.

It is of great importance that the magnetic semiconductor is ferromagnetic above room temperature for practical use. Theoretical calculations of Mn doped semiconductors by Dietl et al. [20] suggested that room temperature DMS could be accomplished in ZnO by large p-doping, see Fig. 3.2. This triggered a large amount of research in this field, which has resulted in many reports of high $T_c$ for many different DMS materials, often above room temperature, but there are also many observations and reports of no ferromagnetism or very low $T_c$ for the same materials. The highest reliable $T_c$ is reported for Mn doped GaAs with $T_c = 173$ K [75, 40]. The experimental situation for DMS is controversial and the high $T_c$ values are often believed to originate from unwanted secondary phases or atomic clusters in the samples. The thesis is mainly devoted to this aspect of DMS, the effect of clustering and unwanted phases in DMS and in particular for Co doped ZnO.

# 4. Magnetism

Two magnets will either attract or repel each other depending on the relative orientation, where the force and associated energy can be described by relatively simple formulas. However, detailed properties of magnetic materials are much more involved and intriguing, which makes magnetism a highly active research field today. In this chapter on magnetism I will briefly discuss some of the core concepts in magnetism that will be required for the continued discussion of the results in my thesis. Textbooks are published on these topics annually and I refer the interested reader either to a classic text like [13] or more contemporary texts on magnetism like e.g. [62, 15].

## 4.1 Is it really so complicated?

It would be nice to provide an easy and insightful model of magnetism but it would probably lack many necessary aspects. It is important to understand that most experimental results, as well as any experience we have of magnetism, can *not* be understood simply by investigating the smallest constituents i.e. the electron and the atom. Usually there is a collective behavior of the magnetic moments, which we refer to as macroscopic or mesoscopic effects, that needs to be considered. Below is a list of magnetic effects which are important and are explained to varying extent.

*Magnetic effects*

Spin magnetic moment of the electron (microscopic)
Orbital magnetic moment of the electron (microscopic)
Spin-orbit interaction (microscopic)
Quenching of the orbital magnetic moment (microscopic)
Crystal field (microscopic)
Exchange interaction (mesoscopic)
Magnetic anisotropy (microscopic, macroscopic)
Demagnetizing field (macroscopic)

The first description of magnetism provided by Maxwell showed a connection between electricity and magnetism called electromagnetism. Basically it describes the magnetic field created by electric charge in motion. It explains the existence of orbital magnetic moments since electrons move in

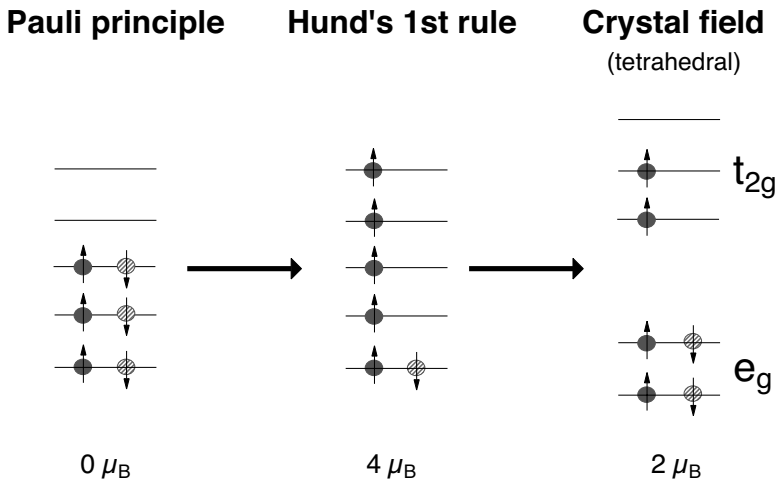


*Figure 4.1.* Illustration of spin ordering in atoms with localized moments. Here 6 electrons occupies the 3d energy levels. The Pauli exclusion principle allows only electrons with opposite spins in the same orbital. According to Hund's 1st rule the atom prefers a high spin state. Crystal field effects alter the energy levels, sometimes enough to force the atom into a low or medium spin state.

orbits around the atomic nucleus. Electrons also exhibit a spin magnetic moment, which is an inherent property of the particle and requires a quantum mechanical description.

In most atoms there are several electrons occupying orbital states around the nucleus. The magnetic moment is cancelled out for all filled electron shells in the atom and it is only necessary to consider the unfilled outer shell. For the 3d transition metals, the outer shell consists of 5 orbital states where each can be occupied by two electrons, see Fig. 4.1. According to the Pauli exclusion principle two electrons in the same orbital must have opposite spins. Due to electrostatic interactions the atom prefers to fill each orbital with electrons having the same spin direction before it begins to occupy orbitals with electrons having the opposite spin direction, this is called Hund's 1st rule. We have illustrated these effects in Fig. 4.1 for an atom with 6 d-electrons. What determines the final magnetic state of an atom is the crystal field effect, which changes the energy levels due to the charge distribution from surrounding atoms. The illustrated energy levels are separated for clarity and does not reflect energy splitting, except for the energy level difference between $t_{2g}$ and $e_g$ states. This effect is often too weak to affect the magnetization as described by Hund's rules, but in some cases it forces the atom into a low or medium spin state.

Hund's 2nd rule suggests a high total orbital moment, precisely as the first rule favors high total spin moment. Unlike the spin magnetic moment, which is often not affected by the crystal field effects, the orbital moment will be

almost completely quenched in the new orbitals created by the crystal field. Due to symmetry breaking at surfaces and particularly at interfaces the orbital moment can be enhanced for thin magnetic films.

## 4.2 Exchange interaction

The energy of a magnetic dipole moment in a magnetic field is described by the Zeeman energy

$$E = -\mu_0 m H \cos(\theta), \tag{4.1}$$

where $\theta$ is the angle between the magnetic moment $m$ and magnetic field $H$. A parallel alignment is preferred since it minimizes the energy. It is often not necessary to have an external field before the magnetic moments arrange themselves in a ferromagnetic order. Since the origin of this ferromagnetic order could not be explained before quantum mechanics was discovered, a phenomenological molecular field model was invented by P. Weiss to explain the experimental results.

Today, it is known that magnetic moments interact between atoms through the exchange interaction. This is not a magnetic interaction but rather a result of reduced Coulomb repulsion between electrons of similar spin, since these can not occupy the same orbital state according to the Pauli exclusion principle. This requires an exchange of electrons between two magnetic atoms, which can mediate the interaction. There are basically four models which describe how this exchange occurs for different types of magnetic materials, see Fig. 4.2.

The double-exchange [86] is an effect of d-electrons hopping between two magnetic ions of different valencies. The hopping occurs through a ligand atom which can accept an electron from the magnetic ion with lower valency if it is has the same spin as the electron which has hopped to the higher valency ion. This promotes a ferromagnetic alignment between the magnetic ions and is a short range interaction.

The superexchange [3] is also short-ranged, basically between nearest neighbors, and in most cases anti-ferromagnetic. It is an effect that comes from two magnetic ions sharing orbitals with the same ligand atom. It might appear similar to double-exchange but it does not involve hopping of loosely bound electrons, which makes this interaction favorable in insulating materials.

The RKKY and the Zener model [20, 85] describe the interaction between charge-carriers and localized magnetic moments of magnetic ions. In a simple picture the charge-carriers (usually *s* or *p* electrons or holes) will experience an exchange interaction with the d-electrons. Since several magnetic ions interact with the same charge carriers, due to their itinerant character, the ground state will usually be ferromagnetic and the interaction more long-ranged than for the double- and super-exchange interactions. The difference between the RKKY

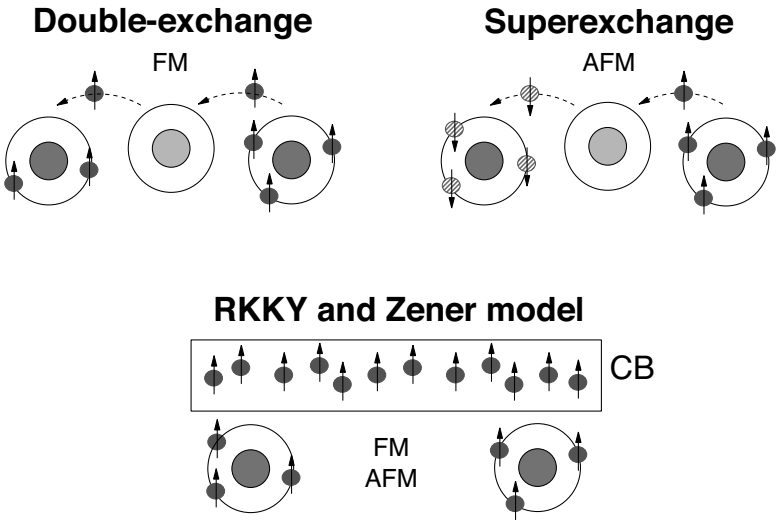


*Figure 4.2.* The exchange interaction is mediated by the exchange of electrons in different ways for different materials. The double-exchange occurs for magnetic atoms with mixed valences. The superexchange is mediated by an oxygen atom and is usually anti-ferromagnetic. The RKKY and The Zener model give a long-range interaction since charge carriers mediate the interaction.

and the Zener model is basically the amount of charge carriers compared to the amount of localized moments. The Zener model works well when there is a larger distance between the charge carriers than between the localized moment and has been successfully used for describing magnetic and transport properties of Mn doped GaAs [19]. The RKKY model is more adapted for describing exchange interactions in metals and has very successfully described the magnetic interaction between FM metal layers in GMR like structures.

## 4.3 Magnetic anisotropy

The ferromagnetic order is also stabilized by different types of magnetic anisotropies, which makes certain directions of the magnetization energetically more preferred than others. The magnetic anisotropy can be divided in two categories, shape anisotropy and magnetocrystalline anisotropy.

The shape anisotropy originates from dipole interactions in mesoscopic and macroscopic magnetic structures. The dipole interaction is very weak between atoms, but for larger structures it can dominate the magnetic behavior in magnetic materials. As illustrated in the top left of Fig. 4.3 the dipole interaction will align two magnets in an antiparallel fashion because the energy from the demagnetizing field will be minimized in this geometry. The competing energies of exchange interaction and demagnetizing field is the reason why many

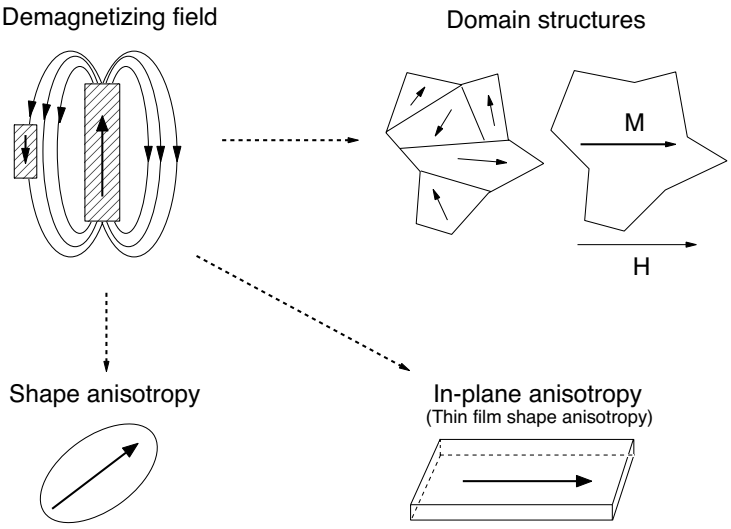


*Figure 4.3.* (Top left) The dipole coupling between two adjacent magnets prefers antiparallel alignment of the magnets. Three effects arise from the demagnetizing field. (top right) The demagnetizing energy is competing against exchange interaction which often leads to domain structures. (bottom left) Nano particles can lower the energy from the demagnetizing field by aligning its magnetization in some preferred direction. Thin magnetic films often have an easy magnetization direction in plane due to the decrease in demagnetizing field.

materials will exhibit domain structures that can be overcome by an applied magnetic field, see top right Fig. 4.3 . This also creates the shape anisotropy found in non-spherical nano-particles and the in-plane magnetization observed in thin magnetic films, see bottom of Fig. 4.3.

Due to the spin-orbit interaction together with the strong connection between the electron orbit and the lattice, the magnetization is strongly effected by the crystal structure, called magnetocrystalline anisotropy. For a cubic crystal the easy axis direction, which is the direction of easy magnetization, depends on the material. For iron with a bcc structure, it is along the principle axes while for Ni it is towards the space diagonal of the fcc lattice. Hexagonal structures exhibit a uniaxial anisotropy with the energy density, expressed as an series expansion in $sin^2\theta$,

$$F = K_1 \sin^2\theta + K_2 \sin^4\theta + ....., \tag{4.2}$$

where $K_1$ and $K_2$ are the anisotropy constants and $\theta$ is the angle between the magnetization direction and the easy axis. Depending on the sign of $K_1$ one either has easy axis or easy plane anisotropy. For thin films the anisotropy constants can be expressed as containing a volume and a surface part

$$K_i = K_i^V + \frac{2K_i^S}{t}, \tag{4.3}$$

where $t$ is the thickness of the film. For very thin films the surface contribution to the magnetic anisotropy will be important and it has been found that the surface magnetocrystalline anisotropy can completely change the easy magnetization direction for ultra-thin films. According to Bruno [10] the difference in orbital magnetic moment for magnetization in the easy and hard axis is proportional to the magnetocrystalline anisotropy. Theoretically, we show that this is not the case for MnAs where the hybridization between Mn and As atoms adds complexity. We do however observe an increase in the orbital magnetic moment along the easy axis due to strain, see Paper VI.

## 4.4 Anti-ferromagnetic nanoparticles: uncompensated spins

The magnetic behavior of a paramagnetic material in a weak applied field can be expressed as

$$M_{para} = N_T \frac{\mu_0 m_{\text{eff}}^2}{3k_B T} H \tag{4.4}$$

where $m_{\text{eff}}$ is the atomic effective magnetic moment, $H$ is the applied field and $N_T$ is the number of atomic magnetic moments per unit volume. The magnetic moment and effective magnetic moment are defined as $m = g\mu_B S$ and $m_{\text{eff}} = g\mu_B \sqrt{S(S+1)}$, respectively, where $g$ is the g-factor and S is the spin. If the atomic moments are clustered and can be described as ferromagnetic nanoparticles with $n_c$ atoms in every cluster the low-field superparamagnetic behavior would give an apparent effective magnetic moment of $n_c m$. The saturation magnetization, $M_s = N_T m$, is the same for both cases.

If the magnetic interaction within these nanoparticles is anti-ferromagnetic, the total particle magnetic moment $m_c$ due to uncompensated spins is according to Neél [56]

$$m_c = n_c^q \cdot m, \tag{4.5}$$

where $q = 1/3$ for uncompensated spins on the surface of the particle.This would give the magnetic moment from the low field magnetic slope $\frac{M}{H}$ as

$$m = n_c^{1/6} \sqrt{\frac{M}{H} \frac{3k_B T}{\mu_0 N_T}}, \tag{4.6}$$

while the magnetization from the saturation magnetization $M_s$ is expressed as

$$m = n_c^{2/3} M_s / N_T. \tag{4.7}$$

Much of the magnetization data obtained for Co doped ZnO are analyzed using this model for anti-ferromagnetic particles and are presented in the summary of results.

# 5. Monte Carlo simulations

Two different computational methods have been used, Density Functional Theory (DFT) and Monte Carlo (MC) simulations. In principle it is necessary to solve the many-body Schrodinger equation $H\Psi = E\Psi$ to fully describe a system. But a macroscopic solid consists of $N \approx 10^{23}$ electrons so it is a computationally impossible task. This problem was solved by W. Kohn and coworkers when they showed that it is sufficient to calculate the electron density n(**r**) instead of dealing with wave functions explicitly [46, 30]. They also developed a self-consistent procedure for obtaining n(**r**) called Density Functional Theory.

All the information obtained from DFT calculations are for systems in the ground state at zero kelvin. To understand how thermal energy effects the system one can use statistical physics which is utilized in MC simulations. In this approach the use of random numbers is essential and it is designed for systems which evolve in a stochastic manner. Statistical mechanics is used

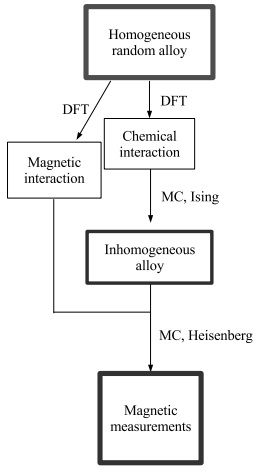


*Figure 5.1.* First the chemical and magnetic interactions are calculated using DFT for a random homogeneous lattice. An inhomogeneous lattice is generated by MC simulation using the chemical interactions as parameters. Finally the magnetic properties for the inhomogeneous lattice are obtained from MC simulations using magnetic interactions as parameters.

for describing how large macroscopic systems behave, in the same way as in classical thermodynamics. One of the main results from statistical mechanics

for a system in equilibrium describes the probability for a system to be in a state $X_v$ if the energy of that state is $E(X_v)$,

$$p(X_v) = \frac{1}{Z} e^{\frac{-E(X_v)}{k_B T}}, \tag{5.1}$$

$Z$ is called the partition function and is closely related to the total energy of the system, $k_B$ is the Boltzman constant and T is the temperature.

The average of an observable $A$ can be expressed as

$$< A >= \int_\Omega p(X_v)A(X_v) \approx \sum_{v=1}^{M} p(X_v)A(X_v) = \frac{\sum_{v=1}^{M} e^{\frac{-E(X_v)}{k_B T}} A(X_v)}{\sum_{v=1}^{M} e^{\frac{-E(X_v)}{k_B T}}}. \tag{5.2}$$

This means that $< A >$ can be approximated by randomly generating $M$ configurations and measuring $A(X_v)$ and $E(X_v)$ for all those states. This method, called simple sampling, is very inefficient for most systems since $p(X_v)$ is usually very peaked so that most states contribute very little to $< A >$. By using a concept called importance sampling it is possible to generate and measure only those states which have a non-vanishing contribution to $< A >$. If the states are sampled with the probability $P_{eq}(X_v) = e^{\frac{-E(X_v)}{k_B T}}$ then the observable reduces to the simple arithmetic average.

$$< A >= \frac{1}{M} \sum_{v=1}^{M} A(X_v). \tag{5.3}$$

The problem is to find a procedure which samples the phase space with the correct probability. This was solved by Metropolis who proposed a simple algorithm. Consider a system in the state $X_i$, now let the system evolve to state $X_j$ with the probability $W_{ij}$ defined as

$$W_{ij} = \begin{cases} 1 & \Delta E < 0 \\ e^{-\Delta E / k_B T} & \Delta E > 0. \end{cases} \tag{5.4}$$

The probability of going from state $X_i \to X_j$ depends on the total energy change $\Delta E = E(X_j) - E(X_i)$ for the system. If the move lowers the energy then it will make the move with probability 1 otherwise it will make the move according to a Boltzmann distribution. It was shown that this algorithm will reach equilibrium after a sufficient number of steps, after which phase space is sampled with the desired $P_{eq}(X_v)$.

We use this scheme to simulate the magnetization at finite temperatures. The energy of the system is obtained from the Heisenberg model

$$H = -\sum_{i \neq j} J_{ij} \hat{S}_i \cdot \hat{S}_j, \tag{5.5}$$

where $J_{ij}$ is the exchange interaction between atom i and j. The exchange interaction is obtained from DFT calculations through a method described by Liechtenstein et al. [49].

## 5.1 Percolation and clustering

Transition metals doped into semiconductors will usually replace a cation atom, e.g., Co replaces a Zn atom in ZnO. The distance through which two magnetic ions can interact is generally short ranged, see Fig. 5.2. Consider now only the nearest neighbor interaction for randomly positioned magnetic atoms in a fcc lattice. It would take at least 20% of the cation atoms to be substituted with magnetic atoms in order to obtain a magnetic "path" through the whole sample, called percolation [8] e.g. a long-ranged magnetic order. Early theoretical calculations performed on DMS systems assumed that the

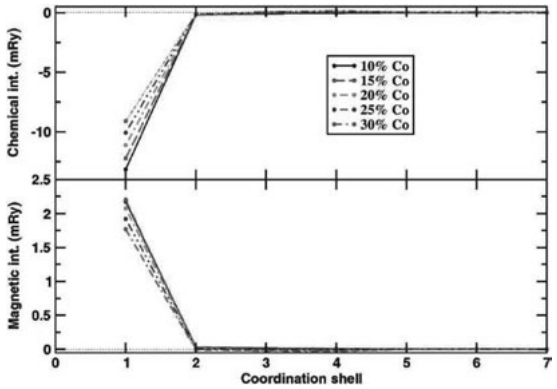


*Figure 5.2.* Magnetic and chemical pair interaction for different Co concentration in Co doped ZnO. Negative chemical potential is an attractive potential between Co atoms and positive magnetic interaction gives a ferromagnetic alignment. From Paper XII.

substitutional magnetic ions are distributed randomly and homogeneously in the semiconductor host. This is generally not a realistic assumption for these materials. We have used a method proposed by Ducastelle [23] to obtain an effective chemical interaction $V_{ij}$ between atoms at position $i$ and $j$.

$$V_{ij} = V_{ij}^{Co-Co} + V_{ij}^{Zn-Zn} - 2V_{ij}^{Zn-Co}, \tag{5.6}$$

where $V_{ij}^{A-B}$ is the potential energy when sites $i$ and $j$ are occupied by atom A and B respectively. The chemical interaction is used in the Ising model to describe the energy of the system

$$H = \sum_{i \neq j} V_{ij}\sigma_i\sigma_j \qquad \text{(Ising model)}, \tag{5.7}$$

where $\sigma_i$ is 1 if the atom at position $i$ is magnetic otherwise it's 0. A Monte Carlo simulation scheme was used with both the magnetic and chemical interaction to describe the effect of clustering in DMS, see Fig. 5.1.

# 6. Experimental techniques: Spectroscopy

Spectroscopy is a collective name for methods investigating either the occupied or un-occupied energy levels available for particles in a material. Except for a few types of atoms, the noble gases, atoms have a tendency to form chemical bonds with other atoms. When an atom becomes part of a compound the energy levels of the outermost electrons, valence electrons, in the atom change as they interact with other atoms. Also, the measured binding energy of core level electrons is affected by what is called a chemical shift. These changes are measured by spectroscopy and gives us a "fingerprint" of which species exists in a solid and how the atoms are bonded to other atoms in its surrounding.

Different types of spectroscopy have been employed. For all cases the sample is subjected to x-rays of varying energy to characterize the absorption of x-rays or the kinetic energy of the emitted electrons. The methods are denoted x-ray absorption spectroscopy (XAS) and x-ray photoelectron spectroscopy (XPS), respectively. X-rays are energetic enough to excite core-levels which is necessary in order to distinguish between different atomic species. However, the kinetic energy of core-level electrons are low when using conventional soft x-ray spectroscopy which results in a high surface sensitivity. Therefore, we have also performed high kinetic energy (HIKE) XPS, when increased bulk sensitivity is required. X-ray magnetic circular dichroism (XMCD) is a spectroscopic variant of the XAS method that is sensitive to the magnetization of samples, which of course is an important tool considering the magnetic nature of our samples.

## 6.1 Synchrotron radiation

Photoelectron spectroscopy is often performed using in-house equipment and is then often referred to as ESCA (Electron spectroscopy for chemical analysis). In many cases this equipment has sufficient intensity and resolution for adequate photoelectron experiments but it is restricted to one photon energy, originating in most cases from the Al $K_\alpha$ emission giving a photon energy of 1487 eV.

A synchrotron consists of a ring, often hundreds of meter in circumference, which is under ultra-high vacuum (UHV). Inside the ring, electrons are circulating with velocities very close to the speed of light. The electron trajectory is controlled by so called bending magnets which forces the electrons into a

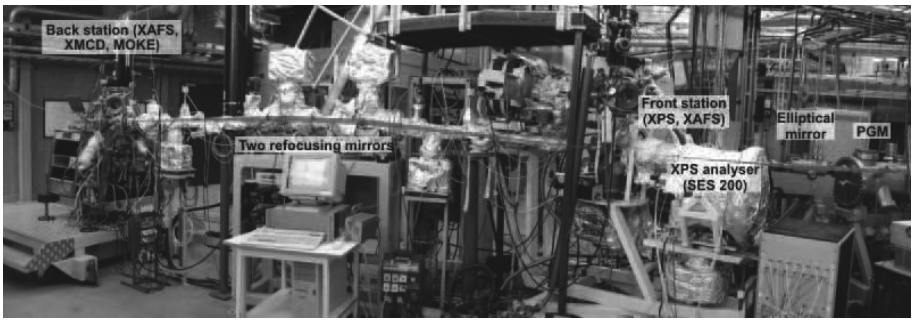


*Figure 6.1.* Beamline D1011 at MAX-lab in Lund. The red line indicates the path travelled by the x-rays [33].

circular path. When a force is applied to electrons moving with high velocity they will emit x-rays. It is this radiation which is utilized in synchrotron facilities. In the first generation of synchrotrons the main source of radiation came from bending magnets but today insertion devices called undulators and wigglers are more common, mainly since they offer higher photon fluxes. For more details I refer the reader to introductory text like Ref. [6].

The radiation produced inside the synchrotron ring travels along a beamline to the end-station where the experiment is performed, the beam-path is indicated with a red line in Fig. 6.1. The beamline and endstation are under ultra high vacuum (UHV) so that the radiation delivered by the synchrotron can reach the sample, since soft x-rays have a short mean-free path in air. Also, the measurements are typically surface sensitive which makes UHV necessary for avoiding surface adsorbates. The construction of the insertion device, beamline and end-station determines which experiments can be performed at a particular beamline. The data presented in the thesis has been collected at several different beamlines. Most of the measurements were performed in MAX-lab at beamline D1011 and I1011 or at the Helmholtz center at beamline KMC-1, also some data is obtained at beamline U4b in NSLS.

## Beamline D1011

This beamline delivers soft x-rays between 30 and 1500 eV from a bending magnet. The beamline is shown in Fig. 6.1 [33]. The monochromator is a modified SX-700 plane grating monochromator (PGM) [61]. The front end-station is positioned directly after the monochromator exit-slit and is equipped with a SCIENTA SES 200 electron energy analyzer used for XPS measurements. A separate preparation chamber is located above the analyze chamber which is connected to a load-lock for easy sample transfer.

Behind the front chamber there is a second chamber which is easily accessible by passing the photon beam through the front chamber. The pho-

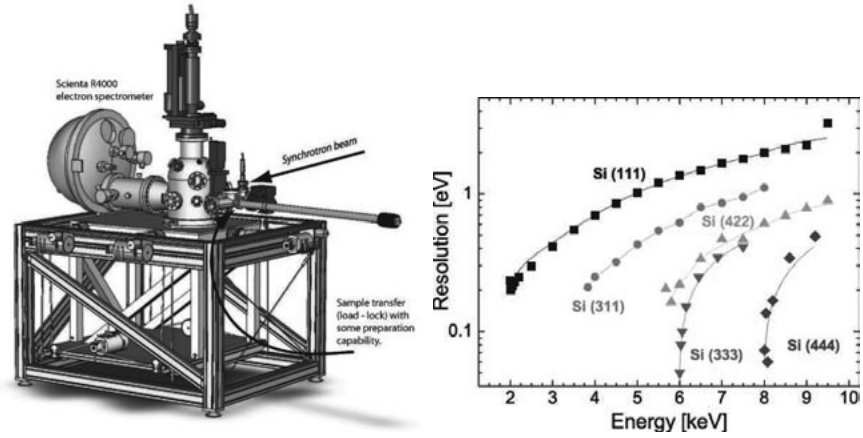


*Figure 6.2.* (left) The HIKE endstation. The Scienta detector, the incoming light and the load lock are marked in the figure. (right) The resolution for different energies as well as for different monochromator crystals. From Paper X.

ton beam goes through a re-focusing mirror system before reaching the back chamber. This chamber is equipped with electromagnets and a multi channel plate (MCP) dedicating this chamber to XAS and XMCD experiments.

## Beamline KMC-1 (HIKE)

The design of this beamline, which is situated at the Helmholtz center in Berlin, is different to D1011 since it delivers x-rays with much higher energy. A grating monochromator is not suitable for hard x-rays and therefore a double crystal monochromator is employed. Depending on the energy, resolution and flux requirements it is possible to change between three different crystals Si (111), Si (311) and Si (422), where a change takes only a few minutes. The end-station is equipped with a VG Scienta R4000 hemispherical electron analyzer. This detector is positioned 90° to the incident light which utilizes the maximum amount of the incident light when the sample is at grazing incidence, while normal emission to the detector maximizes the electron escape depth. The covered energy range is shown in Fig. 6.2 for different monochromator crystals. Using higher order light from the monochromator it is possible to obtain high resolution even at high photon energies, this corresponds to Si (333) and Si (444) in Fig. 6.2. More information about this end-station and beamline can be found in Ref. [26, 27].

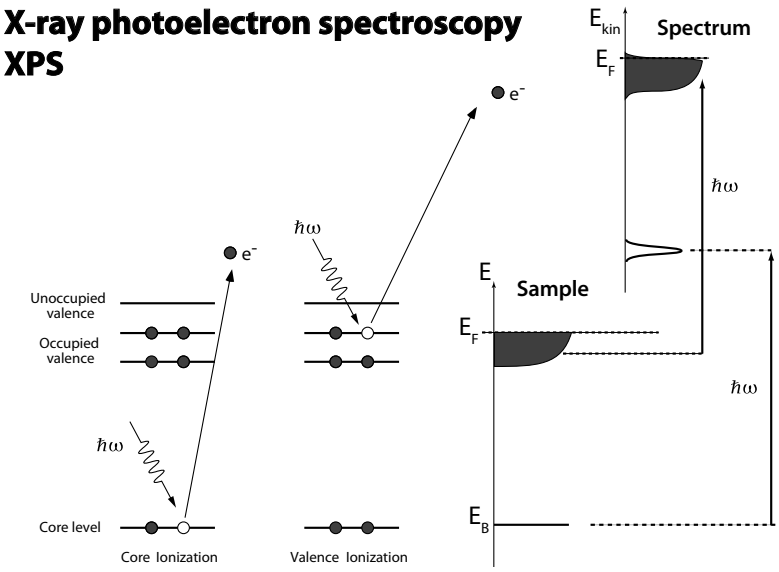


*Figure 6.3.* X-ray photoelectron spectroscopy of core and valence band electrons.

## 6.2 X-ray photoelectron spectroscopy (XPS)

The understanding of the photoelectric process has challanged theoretical physicist for many decades and several key references can be identified (see e.g. Refs. [51, 80, 59, 60, 5, 4]). Several good textbooks also exists on the subject like Refs. [34] and [24]. Atoms (and hence matter) can absorb electromagnetic radiation. If the photon energy is larger than the binding energy of an electron in the atom and the work function combined, electrons will be emitted from the sample with an kinetic energy following equation

$$E_k = h\nu - W - BE \tag{6.1}$$

where $E_k$ is the kinetic energy of the emitted electron, $h\nu$ is the photon energy, W is the work function and BE is the binding energy of the electron. This is Einstein's relation for the photoelectric effect. In metals the Fermi level ($E_F$) is often clearly visible which makes it possible to calibrate the binding energy in reference to $E_F$ even if W is not known. This is often used for semiconducting samples by measuring an Au foil in electrical contact with the sample since the $E_F$ for the metal and semiconductor will align.

The photoelectron emission process is illustrated in Fig. 6.3 where the electron leaves the sample after absorbing a photon, leaving behind an ionized atom [34]. In this one electron picture, the photoelectron emission process of core-level electrons would only provide information on the elemental composition of the sample since the core electrons are very localized and does not take part in any chemical bonding. Fortunately the process is more compli-

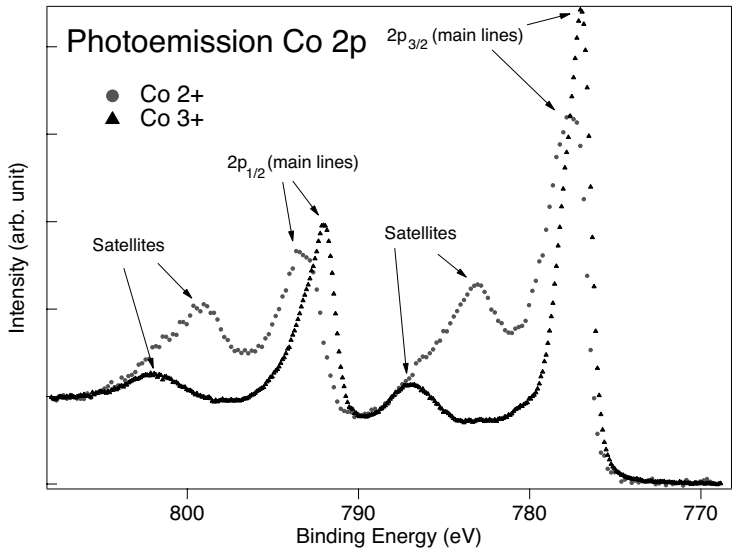


*Figure 6.4.* The photoelectron spectra of Co 2+ and Co 3+ can easily be distinguished. There is both a chemical shift and a large difference in the satellite structure.

cated. Due to initial and final state effects (screening and correlation) a single core level will exhibit chemical shifts and sometimes show additional peaks in the photoelectron spectra which are called satellites. These effects are very sensitive to the chemical environment [18] and can be seen in Fig. 6.4 where we show the Co 2p states for substituted $Co^{2+}$ in ZnO and $Co^{3+}$ in $ZnCo_2O_4$. The main lines of this spin-orbit split core level constitutes a well screen final state in which an electron has been transfered from the ligand valence band, denoted L, to the Co 3d state. The satellite structures are due to less screened states, these two types of final states are denoted as $2p^5 3d^8 L^{-1}$ where $L^{-1}$ is a hole in the ligand valence band and $2p^5 3d^7$ respectively. In addition to the different spectral shapes there is also a chemical shift between the main lines. Therefore this method is often very efficient for determining the chemical valency of atomic species.

There are basically two different regions which are studied using photoelectron spectroscopy, core-levels and the valence band. Most of the properties (magnetic, optical, electronic transport, heat transport, catalytic) which are of interest in a solid are strongly connected to the valence band structure. The main difference is that valence band electrons are not as localized as core level electrons and are able to hybridize, meaning that the valence band states of atoms mix. The valence band and in particular the position of the 3d states of the magnetic atom is important when trying to identify the mechanism which could result in ferromagnetic properties and for comparison to theoretical results.

## Resonant photoelectron spectroscopy (RPES)

If the valence band photoelectron emission is recorded using a photon energy which corresponds to an absorption edge, we will experience an interesting phenomena called resonant photoelectron emission. In this case the photon can be absorbed creating either a direct photoelectron event of a valence band electron or by exciting a core electron into an empty conduction band state. In the latter case, the atom may relax by filling the core hole with an electron from the valence band and emit an electron from the valence band.

For a Co atom excited with a photon energy corresponding to the $L_3$ edge we have

$$2p^6 3d^7 + \hbar\omega \rightarrow 2p^6 3d^6 + e^- \qquad \text{(photoelectron)}$$

$$2p^6 3d^7 + \hbar\omega \rightarrow 2p^5 3d^8 \rightarrow 2p^6 3d^6 + e^- \qquad \text{(absorption and autoionization)}$$

in which we observe that the final state is identical for both direct photoelectron emission and for the autoionization [9]. The cross-section for absorption is generally much higher than for direct photoelectron emission of valence band electrons at these energies. Therefore the total cross section for valence band states corresponding to atoms which have an absorption edge at the used photon energy is strongly enhanced. This effect is shown in Fig. 6.5 where a large increase in intensity is observed for Co 3d states at the valence band edge for resonant energies compared to off-resonant. It should be noted that this is a simplified picture of the resonant process. Since the initial and final states are identical, the two different processes can not be separated and only a complete quantum mechanical treatment, taking the possibility of interference into account, can correctly describe the resonant spectra [78].

## High kinetic photoelectron spectroscopy (HIKE)

The surface sensitivity of XPS is valuable for many types of experiments but it can also be problematic when bulk properties are sought. Often samples needs to be prepared *in situ* to minimize contributions from surface contamination. If the sample is sensitive to oxidation it needs to have a protective capping layer or the top layers will not be representative for the bulk properties, in either case the top layers needs to be removed which is difficult without affecting the sample. To study structures which are buried deeper than a few nm is not possible using traditional XPS [31, 38, 41, 26, 27].

According to the universal curve (see Fig. 6.6), the mean free path (MFP) of electrons can be increased by using electrons with high kinetic energies and it also indicates that the MFP is relatively material insensitive. A high kinetic energy of the electron can be obtained by exiting the photoelectron with high photon energies. The use of hard x-rays for XPS actually predates the use of soft x-rays in the 1950's due to difficulties in transmission of low en-

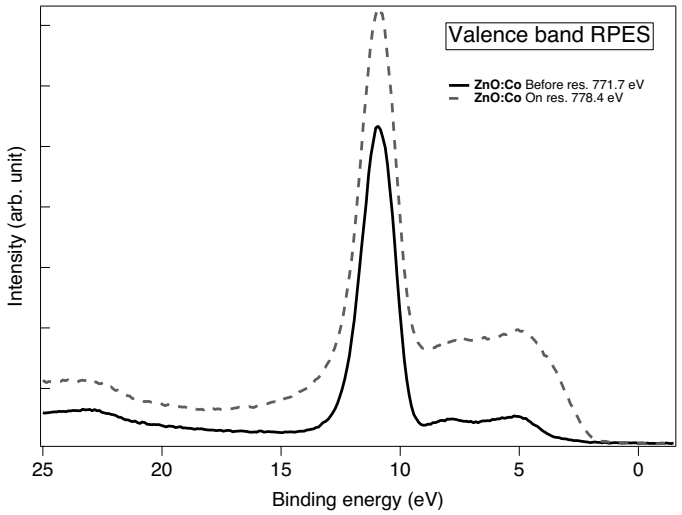


*Figure 6.5.* Valence band of 5% Co doped ZnO obtained with two different photon energies. With 778.4 eV photon energy, which corresponds to the $L_3$ absorption edge of Co, there is a strong increase in intensity at the VB edge due to the presence of Co 3d states.

ergy electrons in the detectors. In 1960's the development of detectors, spectrometers and soft x-ray sources led to large advances in soft-x photoelectron spectroscopy. During the last decade there has been a large increase in the use of HIKE, where hard x-ray photoelectron spectroscopy (HAXPES) is a common synonym. This is mainly due to advances in the engineering of good energy analyzers capable of handling high kinetic electrons with high resolution. Also, new synchrotron sources and monochromators with high resolving power in the hard x-ray region have been necessary to enable the full power of this technique.

Hard x-ray photoelectron spectroscopy can be used for studying core-levels with high binding energy but the main use has been to study core-levels which are available even with soft x-rays but with a much higher bulk sensitivity. With photon energies usually between 2-12 keV, HIKE presents the opportunity to study interface diffusion within metallic multilayers. The electron binding energy of core levels is very sensitive to the chemical environment of the atom. A shift in binding energy, also called chemical shift, occurs due to changes in the screening of the positively charged core hole as the nearest environment of the atom is affected due to diffusion. As an example we show the chemical shift of Rh in the Heusler $Rh_2CuSn$ as the sample is annealed at various temperatures in Fig. 6.7. The screening of the core hole depends on the hybridization with the surrounding atoms and requires DFT calculations for a quantitive modeling.

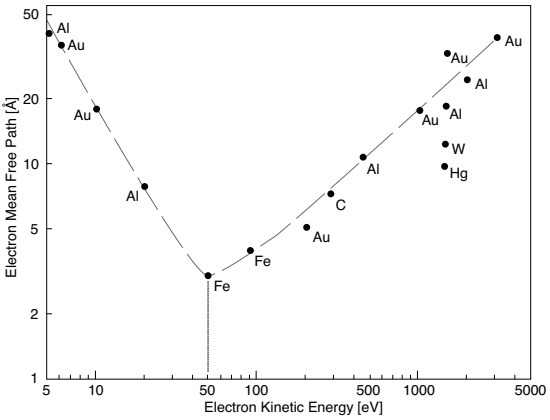


*Figure 6.6.* The universal curve which illustrates the mean free path (MFP) of electrons in solids as a function of the electron kinetic energy. The MFP is relatively material insensitive and higher kinetic energies increases the probing depth, for energies larger than 50 eV.

We have used HIKE to study bi- and multi-layers of CoFeB/MgO, Cu/Ni, Fe/V and CoMnGe/RhCuSn. The chemical shift after heat treatment as well as for different layer thicknesses has been studied. Using this method we are able to follow the diffusion of different constituents, including the cap layer.

## 6.3 X-ray absorption spectroscopy (XAS)

X-ray absorption spectroscopy (XAS) is a very powerful technique that is used in many different areas where understanding of electronic structure is relevant. For a more complete appreciation of the capabilities the techinique offers I refer the reader to e.g. the book by Stöhr [72]. Unlike photoelectron spectroscopy which excites electrons into the continuum, XAS excites core level electrons into unoccupied energy levels [18]. The absorption probability is proportional the number of available states and XAS is thus a method for probing the unoccupied density of states at a given energy. It is performed by scanning the photon energy corresponding to a particular core level excitation to the empty conduction band. The intensity of the light is measured both before and after the light has been transmitted through the sample. The intensity of the transmitted light $I$ is related to the absorption cross-section

$$I = I_0 e^{-\mu x} \tag{6.2}$$

where $I_0$ is the intensity of the impinging light, $x$ is the sample thickness and $\mu$ is the absorption cross-section which depends on the x-ray energy. Since the intensity of the transmitted light decreases exponentially with the sample thickness, this type of experiment can only be conducted for thin samples.

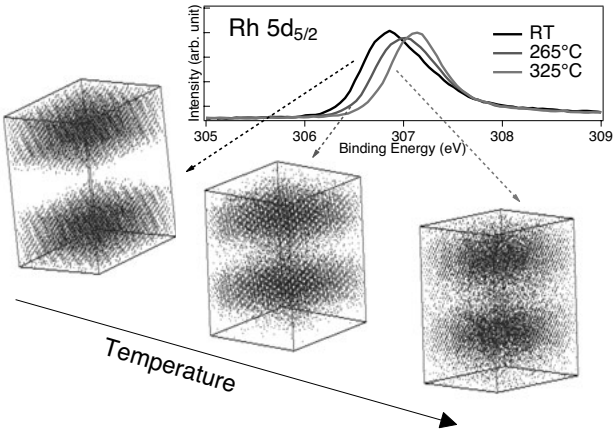


*Figure 6.7.* An illustration of the chemical shift in Rh $5d_5/2$ as the multilayer structure is destroyed by diffusion, induced by annealing.

Instead it is common to use a more indirect way of measuring the absorption cross-section. When a highly excited atom relaxes, it decays either by electron emission or photon emission, see Fig. 6.8. For core levels accessible by soft x-rays the electron emission is much more probable to occur. Therefore a simple and common method for obtaining the absorption cross-section is to measure the number of secondary electrons leaving the sample. This is done either by measuring the current between ground and sample or by registering the emitted electrons using a multi-channel plate (MCP).

The absorption process is not as sensitive to charge transfer effects as XPS but is more sensitive to multiplet effects. Multiplet structures are observed in atoms with localized valence band electrons and appear due to the strong overlap of wave functions between the core hole and localized 3d electrons. This makes it very simple to distinguish between metallic and ionic states for 3d transition metals since metallic states does not show multiplet features due to their delocalized nature.

## 6.4 X-ray magnetic circular dichroism (XMCD)

Magnetic measurements are often performed using a Superconducting Quantum Interference Device (SQUID) which offers a quick, very sensitive and relatively easy method to obtain magnetization data. The drawback is that it offers no information about the origin of the magnetic response. This is one of the main strengths of XMCD.

X-ray absorption has different cross sections depending on the polarization of the light. In the case of circularly polarized light the cross-section is sensi-

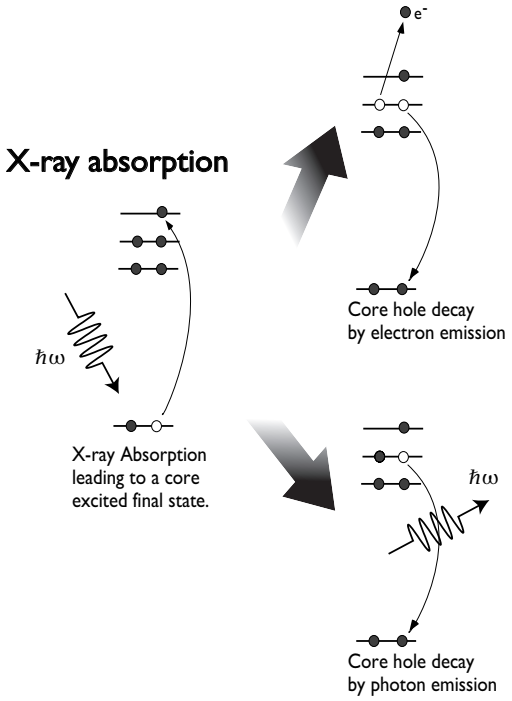


*Figure 6.8.* X-ray absorption as a two-step process. (left) A core electron is excited to the an unoccupied state. (top right) The atom relaxes by electron emission or (bottom right) photon emission.

tive to both the magnitude and direction of magnetization in the sample. The difference in absorption between right and left handed circular polarized light is called XMCD. The experiments are performed either by switching between left ($\sigma^-$) and right ($\sigma^+$) handed circularly polarized light or by changing the magnetization direction of the sample, both methods are identical. An illustration of the XMCD process is shown in Fig. 6.9.

Circularly polarized light carries an angular momentum which is either in the direction of motion or opposite to it, $\sigma^+$ (+$\hbar$) and $\sigma^-$ (-$\hbar$) respectively. Usually the angular momentum from a photon can only be transferred to the electrons orbital momentum and thus conserving the spin of the electron. For electrons which experience a strong spin-orbit coupling, as for 2p electrons in transition metals, the orbital and spin quantum numbers are no longer good quantum numbers and the spin is not necessarily conserved. For right polarized light at the $L_3$ edge 62.5% of the excited electrons are spin up while the same holds for left polarized light but now for spin down electrons. Since the absorption cross-section is proportional to the number of empty 3d states and magnetic materials have more unoccupied states in one spin direction than the

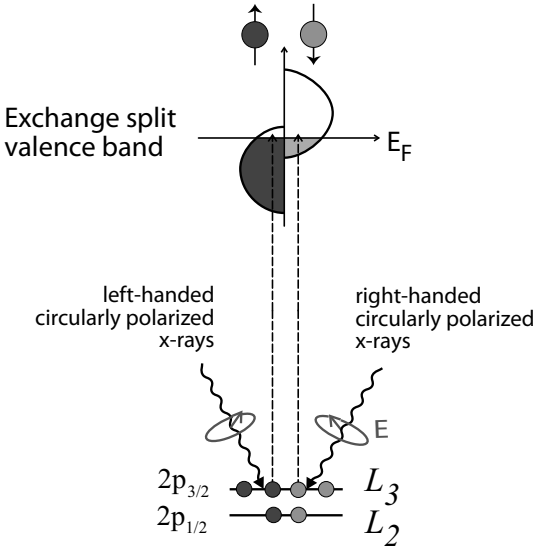


*Figure 6.9.* Right handed circularly polarized light excites more spin up electrons than left handed at the $L_3$ edge. This enables us to measure the difference in occupied spin up and spin down 3d states with XMCD.

other; it follows that the absorption of circularly polarized x-rays are sensitive to the magnetization of the sample.

Even though this method works for all atoms which have a net magnetic moment it has turned out to be very useful for transition metals, in particular for the $L_{2,3}$ absorption edges. It was shown by Thole et al. [73, 12] that both the spin- and orbital-magnetic moment can be derived from XMCD spectra obtained from the $L_{2,3}$ absorption edges. Simple formulas for deriving the magnetic moments exists which are called XMCD sum rules and are discussed in the next section.

## XMCD sum rules

In some cases it is straightforward to obtain both spin and orbital magnetic moments from XMCD data by using magneto-optical sum rules [12, 73]. The magnetic moments are obtained as Bohr magnetons per atom and therefore no prior knowledge of the samples, as the thickness or concentration of magnetic ions, is necessary. The sum rules are

$$m_s = -C\frac{3p-2q}{r} + \frac{7}{2} < T_z > \tag{6.3}$$

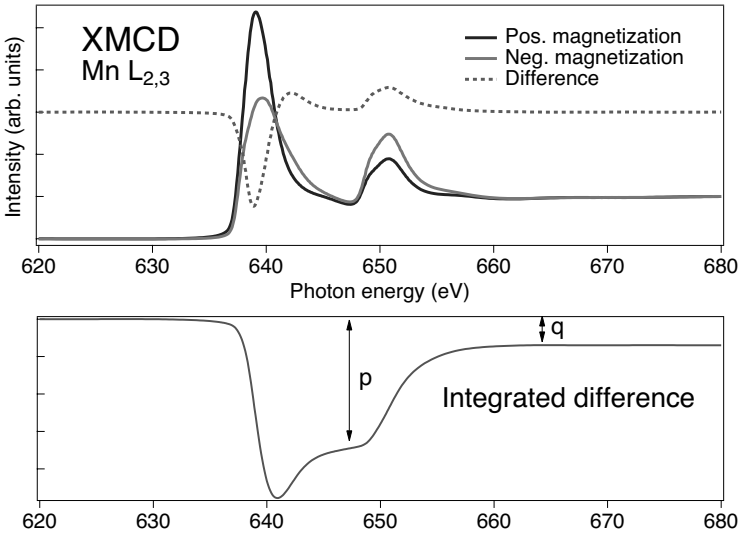


*Figure 6.10.* (Top) Mn $L_{2,3}$ XMCD. The absorption is obtained after pulsing with a saturating field. (bottom) Integration of the difference obtained in the top graph. The values p and q are used in the sum rules.

$$m_l = -C\frac{2q}{3r} \tag{6.4}$$

$$\frac{m_l}{m_s} = \frac{2}{9\frac{p}{q} - 6} \tag{6.5}$$

where $m_s$ and $m_l$ are the spin and magnetic moments respectively. $T_Z$ is the intra-atomic magnetic dipol operator which in most cases can be approximated as $< T_Z >= 0$. For low symmetry situations as for thin films $< T_Z > \neq 0$ but can then be estimated by angle dependent XMCD [79] or by calculations. C is a constant which involves the angle between the incident light and magnetization direction of the sample and is also proportional to the number of empty 3d states. The constants p and q are obtained from the XMCD spectra, see Fig. 6.10, where p is the integrated difference of the $L_3$ edge, q is the total integrated difference between the spectra. The value of r is the average total integrated intensity of the absorption edges after a step background has been subtracted.

## Time resolved XMCD

The photons which are delivered from a synchrotron originate from electron bunches and hence are delivered to the end-station as photon flashes of a certain length. At the MAX-II synchrotron the bunch length is 650 ps (FWHM). Usually the synchrotron radiation can be viewed as a continuous stream of

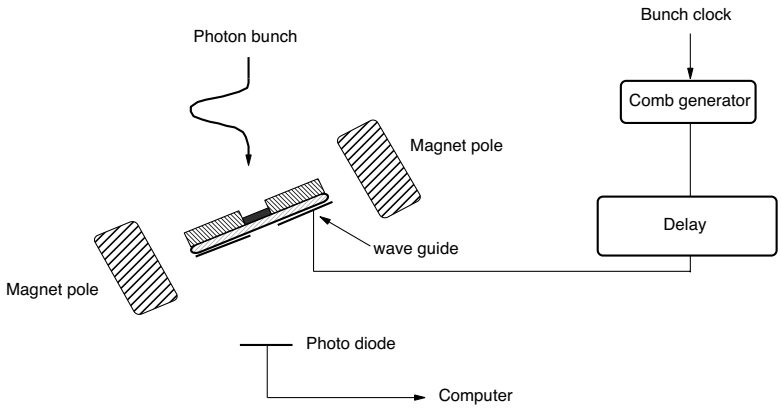


*Figure 6.11.* Experimental setup for time resolved XMCD.

photons since $10^8$ bunches reach the sample every second. However, the bunch structure can be utilized for pump-probe experiments where ferromagnetic resonance (FMR) acts as the pump and XMCD as the probe.

Ferromagnetic resonance uses microwaves to produce an oscillating magnetic field in the GHz regime. This magnetic field will force the magnetic moments in magnetic materials to oscillate with the frequency indicated by equation 6.6 at the resonant bias field $H_{res}$.

$$f^2 = (\mu_0\gamma/(2\pi))^2 H_{res}(H_{res} + M_S) \tag{6.6}$$

where $M_s$ is the saturation magnetization, $\mu_0$ and $\gamma$ are the vacuum permeability and gyromagnetic ratio, respectively. The experimental setup is illustrated in Fig. 6.11 where the bunch clock, which is phase locked to the photon bunches and has a frequency in the order of 100 MHz, generates through higher harmonics a microwave output from a comb generator (a overtone spectrum generator). The microwave signal goes through a delay line which can be controlled down to 5 ps. The delayed microwave signal then arrives to a coplanar waveguide which is situated as close to the sample as possible for maximal magnetic field at the sample. For transmission geometry the sample needs to be grown on a thin substrate which is transparent to x-rays. This is illustrated in Fig. 6.11 where the sample (solid black) is grown on a small SiN window. The intensity of the transmitted light is registered by a photodiode and collected in a computer. If the photon energy corresponds to a magnetically sensitive core level the transmitted intensity will depend on the phase of the spins as the photon bunch is transmitted, which is controlled by the delay line. The setup also contains amplification steps and use of lock-in amplifiers to increase the signal-to-noise ratio but these are omitted for clarity.

# 7. Summary of papers

## 7.1 Dilute magnetic semiconductors

The earliest publications included in this thesis describe work focussed on electronic structure calculations and magnetic percolation in dilute magnetic semiconductors. The goal was to understand under which conditions transition metal doping could induce FM coupling in semiconductors. On the experimental side the most important part of this research was reliable sample preparation and characterization in order to accurately deduce the magnetic interactions involved. Several different parameters have been varied for Co doped ZnO such as post-annealing, co-doping, synthesis method and doping concentration to get a more profound understanding of this compound.

### Electronic structure (Papers I, II, III, IV)

The electronic structure of transition metal doped ZnO has been studied by XAS, XPS and RPES. The differences in electronic structure between ZnO samples with low (5%) and high (15%) doping levels of Co will be summarized below. Also, the sensitivity of Fe reduction due to x-ray exposure, which was not an issue for Co doping, will be discussed.

The valence band in Fig. 7.1 (left) is shown for samples with and without 5% Co doping and 0.8% Al co-doping. The Co doped samples show additional states at the valence band edge. RPES confirms that these states are of Co 3d character, shown in Fig. 6.5, where an intensity increase is observed at the VB edge for energies corresponding to the Co $L_3$ absorption. It is found that the Fermi level is not effected by Al co-doping, which should act as an *n*-dopant. This suggests that the Fermi level is pinned at the conduction band edge by intrinsic n-dopants like oxygen vacancies already for non Al doped samples. These results can be compared to the valence band obtained for samples with high (15%) Co doping in Fig. 7.1 (right). The samples have been post annealed at various temperatures. Only the sample annealed at 800° C show a similar shape as for the low doped samples, with additional states at the valence band edge. All other samples also have states in the band gap.

From the RPES shown in Fig. 7.2 (left) for the 400° C sample we obtained the partial absorption spectra shown in Fig. 7.2 (right). This method can resolve the Co $L_3$ absorption for different chemical species if the valence electrons are separated in binding energy. This is the case for substituted Co found

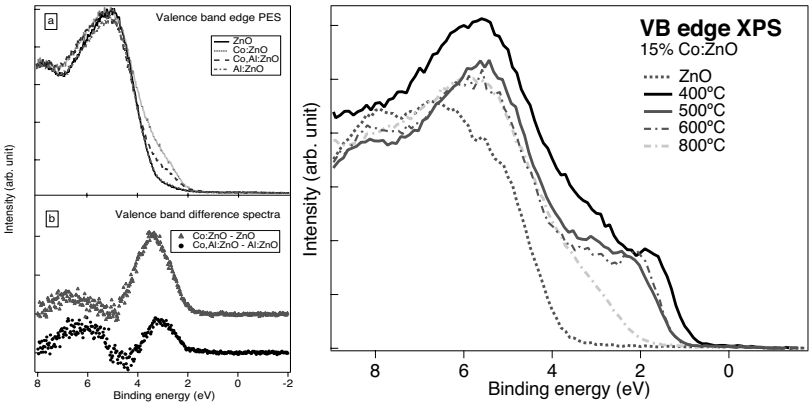


*Figure 7.1.* (left) The VB with and without 5% Co and 0.8% Al doping. (right) 15% Co doped ZnO which exhibit band gap states for all post annealed temperatures except 800°C.

at the valence band edge and the states found in the band gap. The partial absorption of the band gap states (solid orange) is very similar to the absorption of $Co_3O_4$ spinel (black dotted). X-ray diffraction (XRD) shows no indication of $Co_3O_4$ or $ZnCo_2O_4$ for the 400° C sample, while spectroscopy suggests a large amount of these secondary phases. This might be due to a small crystal size of the secondary phases rendering them invisible to XRD or that the samples contain a large amount of Co 3+ which has not relaxed into the spinel structure. A weak spinel signal is found for the 500° C and 600° C samples by XRD.

The Co $2p_{3/2,1/2}$ core levels for the 15% Co doped sample in Fig. 7.3 (right) could be fitted well using the data obtained from the 5% Co doped sample, which correspond to $Co^{2+}$ substituting Zn (dotted red), and from the very highly doped (35%) Co doped ZnO (black). The 35% sample has a pure $Co^{3+}$ character which suggests that all Co visible to XPS have formed a $ZnCo_2O_4$ spinel. It is found that a good fitting is only possible by adding a third component having the same spectral shape as $Co^{2+}$ but shifted to a higher binding energy (solid blue). The origin of this component is unknown but the substituted component is approximately constant through the temperature series, while the unknown component increases when the $Co^{3+}$ decreases and vice versa. Since Co spinel is formed due to clustering of Co atoms and magnetization data also indicate cluster formation, it is reasonable that the two different $Co^{2+}$ components could be explained by the different chemical environment for Co in the bulk and on the surface of clusters.

We used Co implantation of single crystal ZnO as an alternative route for achieving high doping concentrations while maintaining a phase pure ZnO sample. The Co concentration is found, by secondary ion mass spectrometry (SIMS), to be about 10% within 30 nm from the surface. The implanted sam-

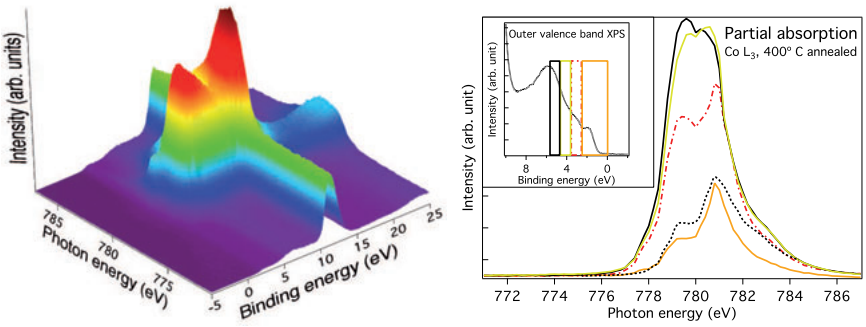


*Figure 7.2.* (left) Valence band RPES spectrum of the 400°C sample. The valence band was recorded with photon energies ranging across the Co $L_3$ edge. (right) Partial absorption of the Co $L_3$ edge. The absorption was constructed by integration over specific BE ranges from the RPES spectrum. The inset shows the VB XPS and the boxes indicate which BE ranges have been integrated.

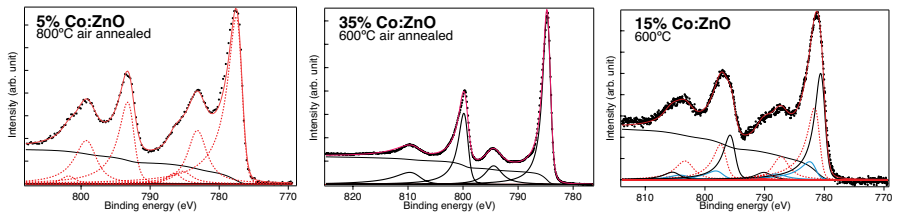


*Figure 7.3.* Core level XPS of Co 2p. The left graph shows a spectrum for a 5% Co doped ZnO sample which is used as the model spectrum of substituted $Co^{2+}$. Middle graph is a spectrum of 35% Co doped ZnO sample which is used as a model spectrum for pure $Co^{3+}$. The right graph shows the spectrum for a 15% Co doped ZnO sample fitted using the model spectra corresponding to $Co^{2+}$ (dashed red), $Co^{3+}$ (solid black) and an unknown $Co^{2+}$ component (solid blue).

ples were heated to 500°C and 800°C in an Ar atmosphere. The as-implanted sample had a thick carbon layer on the surface, which rendered x-ray spectroscopic measurements impossible for this sample. Co implantation induces a high amount of disorder in the single crystal ZnO substrate, which was to a large extent cured by annealing at 800°C according to Rutherford backscattering spectroscopy (RBS). Since the Co concentration peaks at about 20 nm below the surface, we used high kinetic energy photoelectron emission to increase the probing depth. The valence band, obtained using a photon energy of 4 keV, see Fig. 7.4 (left), indicates additional states at the VB which we have shown earlier to be from Co substituting Zn. The intensity of these states decreases as the sample is heated to 800°C, which is consistent with a Co diffusion into the bulk as found by SIMS. Also, we observe states in the band gap for the 800°C annealed sample which were assigned earlier to $Co^{3+}$. The

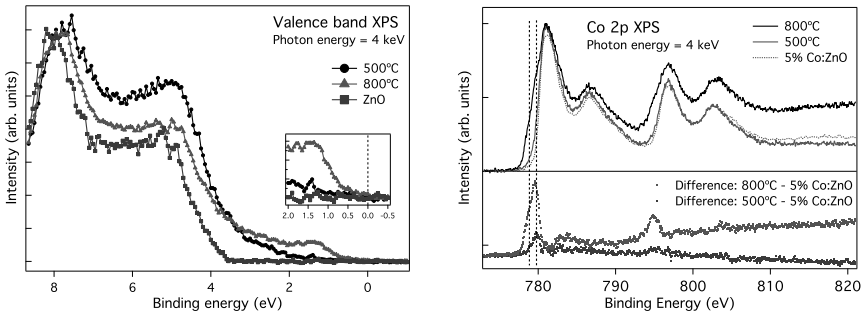


*Figure 7.4.* (left) The VB obtained with high kinetic photoelectron spectroscopy (HIKE) indicates a phase pure sample after 500°C annealing but after 800°C annealing the inclusion of both $Co^{3+}$ and metallic Co become apparent. (right) The Co 2p core level confirms the existence of secondary phases.

inset shows that this sample has states at the Fermi level, which suggests that some of the Co has reduced to metallic Co. This is confirmed by Co 2p XPS in Fig. 7.4 (right) where the 500°C sample is almost identical to the phase pure 5% doped sample, while the 800°C sample shows two additional peaks at the low binding energy side corresponding to $Co^{3+}$ and metallic Co [28, 14].

We have also doped ZnO with Fe using a wide concentration range from 1% to 10%. Even though we initially intended this to be a study of magnetic semiconductor properties it turned out to be of interest for photocatalytic properties in ZnO, as well [83, 21, 22]. We found that Fe prefers a 3+ oxidation state in these samples but x-ray exposure will reduce the Fe to a 2+ state. In Fig. 7.5 (left) we have measured the Fe $L_3$ absorption edge for the 2% Fe doped sample. The peak around 709.7 eV photon energy corresponds to $Fe^{3+}$ while the peak around 708.4 eV is from $Fe^{2+}$ [81, 74]. The arrows indicate how the peak intensities change after x-ray exposure, the $Fe^{3+}$ decreases at the same rate as the $Fe^{2+}$ increases which means that the iron is reduced. The inset shows the partial electron yield (PEY) which is more surface sensitive than total electron yield (TEY) indicating that the reduction occurs near the surface. The reduction is observed for all Fe concentrations, shown in Fig. 7.5 (right), where we have plotted the $Fe^{2+}$ fraction as a function of x-ray exposure time. The $Fe^{2+}$ fraction is lower for higher Fe doping concentrations which is due to a lower amount of Fe on the surface than the nominal concentration. The $Fe^{2+}$ is oxidized to $Fe^{3+}$ after air exposure. The reduction of Fe occurs likely due to the creation of oxygen vacancies, which have been shown to be produced at the surface by UV radiation [48].

Similarly as for Co doped ZnO we observe states in the ZnO band gap. Using resonant photoelectron emission we studied the partial absorption of the Fe $L_3$ edge, the results are shown in Fig. 7.6. The baseline of the partial absorption corresponds to the binding energy in the RPES spectrum on the

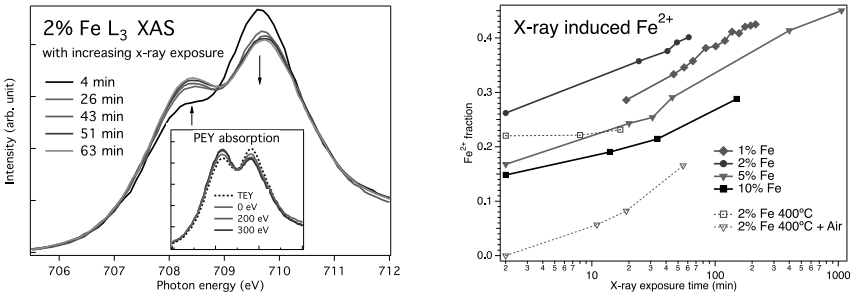


*Figure 7.5.* (left) Fe $L_3$ XAS after different x-ray exposure times. The intensity at 709.7 eV decreases while it increases at 708.4 eV which correspond to a reduction of $Fe^{3+}$ to $Fe^{2+}$. (right) The reduction occurs for all Fe concentration.

right, from which the partial absorption was obtained. The band gap states, spectrum A1, have a photon energy corresponding to $Fe^{2+}$ which is likely in a low spin state since it does not have the multiplet structure usually found for $Fe^{2+}_{HS}$ as in spectrum A4 [81]. Deeper in the valence band we observe an intensity increase of $Fe^{3+}$ states.

The reduction of transition metals ions in oxides by x-rays has to our knowledge not been reported before and the implications may be important since x-ray spectroscopy is a common characterization method for these types of materials. Especially, Fe doped ZnO is often characterized as containing a mixture of $Fe^{2+}$ and $Fe^{3+}$ [42, 47, 25]. This effect is also very interesting for understanding photocatalytic properties of ZnO where Fe doping has been shown to increase the efficiency, supposedly due to a narrowing of the band gap [83, 21, 22].

## Theory of interactions and percolation in DMS (Papers XII, XIII, XIV)

Magnetic and chemical pair potential parameters were obtained by DFT calculations for Mn doped GaAs and Co doped ZnO. The chemical pair potential parameter is negative for nearest neighbor Co atoms indicating an attractive potential and the magnetic interaction is positive and hence ferromagnetic. Spinodal decomposition is an effect which can be observed when a system is cooled down fast, i.e quenched into a solubility gap. The different constituents do not have the possibility to form segregated phases but instead local density fluctuations will be amplified. Using the chemical potential as a parameter, we have used Monte Carlo simulations to simulate spinodal decomposition. The change in magnetization after spinodal decomposition has also been obtained by Monte Carlo simulations, using the Heisenberg model.

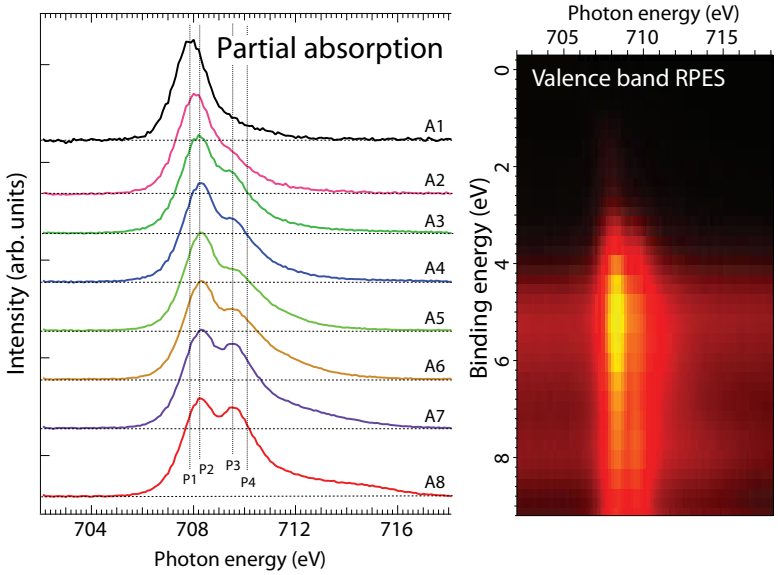


*Figure 7.6.* The partial absorption of Fe $L_3$ obtained from the resonant photoelectron spectrum on the right side. Band gap states corresponding to spectrum A1 are likely from low spin $Fe^{2+}$, spectrum A4 corresponds to high spin $Fe^{2+}$. $Fe^{3+}$ states are mainly found deeper in the valence band (A6 - A8).

In Fig. 7.7 we have simulated the magnetization for 5% Mn doped GaAs. Every magnetization curve corresponds to a certain number of Monte Carlo steps (MCS) performed during the spinodal decomposition simulation. MCS can be viewed as the time frame in which the atoms are allowed to move in the lattice. Very early in the simulations there is an enhancement in $T_C$ but after a few 100 MCS the system becomes superparamagnetic and the clusters are easily seen in the inset.

A similar behavior is also observed for 10% Co doped ZnO, see Fig. 7.7, where the superparamagnetic signature can be seen after 2000 MCS. The nearest neighbor magnetic interaction is similar for Co doped ZnO as for Mn doped GaAs. However, the latter has more long-ranged interactions which result in a much higher $T_C$ for the random homogeneous (0 MCS) sample. The long-range interaction in Mn doped GaAs has been explained by the Zener model where holes (Mn is a p-dopant in GaAs) are responsible for mediating the long-range interaction [20, 85]. The 30 % Co doped sample does not become superparamagnetic and actually shows a large increase in $T_C$ for all cases. This indicates that magnetic percolation is obtained through the lattice. The strong nearest-neighbor interaction becomes active for more of the atoms for every MCS, increasing the $T_C$.

A drawback for these calculations is that interactions are calculated using a coherent potential approximation (CPA). This method calculates the magnetic

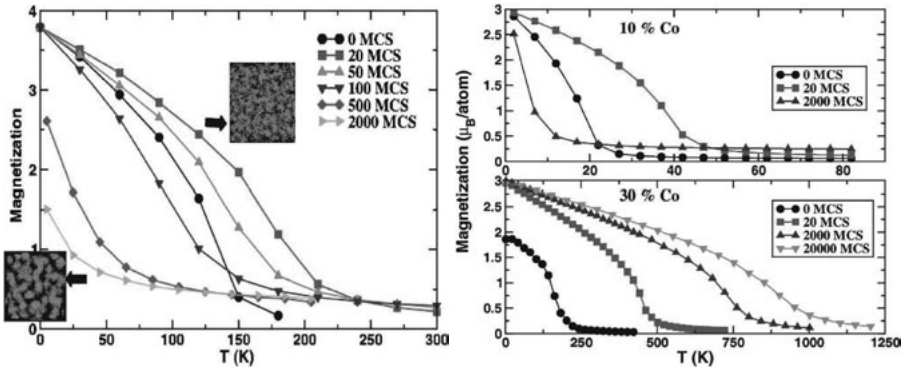


*Figure 7.7.* Monte Carlo simulations of (left) 5% Mn doped GaAs. The different magnetization curves correspond to the number of Monte Carlo steps performed. (right) Co doped ZnO. The $T_C$ is very low for 10% Co doping and the system eventually becomes superparamagnetic. For 30% Co doping the system is ferromagnetic at all times.

and chemical interaction between two magnetic atoms which are in an average environment of Co and Zn and does not take into account any local effects [69]. More recent calculations, which are sensitive to the local densities, are discussed in the next section.

## Magnetic interactions (Papers I, II, III, V)

According to DFT calculations, where the coherent potential approximation has been employed, the magnetic interaction is very short-ranged and mainly ferromagnetic except for high Co concentrations where the next nearest neighbor interaction becomes anti-ferromagnetic. This scenario would have a close correspondence to CoO which is a known anti-ferromagnet. More recent supercell calculations [36] using LDA+U suggest that the nearest neighbor interaction between Co atoms in ZnO is mainly anti-ferromagnetic.

As was discussed in the electronic structure section, some of the 15% Co doped samples contain spinels but the low doped samples show no indication of secondary phases, neither in XRD nor in x-ray spectroscopy. The magnetization data of these samples, measured by SQUID magnetometry (see Fig. 7.8 ), show no remanence nor coercivity at any temperature. The saturation magnetization is lower than what is expected from $Co^{2+}$ which should be 3 $\mu_B$. For all samples the magnetization vs. temperature show a Curie behavior with no indication of blocking temperatures. The effective magnetic moments can be calculated from the low field slopes and are presented in table 7.1 for the 15% Co samples. The effective magnetic moments are in all cases much higher than the saturation magnetic moment which suggests that the samples do not exhibit a paramagnetic behavior. It is also clear due to the absence of

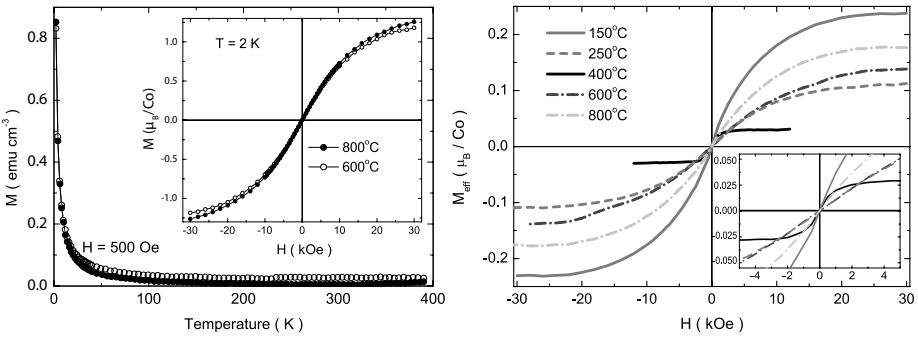


*Figure 7.8.* SQUID magnetization at 2 K. (Left) 5% Co doped ZnO annealed at two different temperatures. (Right) 15% Co doped ZnO. All curves have a paramagnetic like behavior with no remanence or coercivity.

coercivity, remanence and low saturation magnetic moments that there are no long-ranged ferromagnetic interactions.

The only interaction which has not been ruled out is the anti-ferromagnetic interaction. It has been argued earlier that Co has a propensity to aggregate in ZnO. We therefore use a model by Néel [56] to describe the magnetic behavior for anti-ferromagnetic Co clusters with uncompensated spins. According to this model we can calculate the cluster size from the saturation magnetic moment or the effective magnetic moment. The results are presented in table 7.1 for the 15% Co doped samples. The same model is also used for the 5% Co doped samples by which the cluster size is estimated to be about 5 atoms.

| Annealing temp. | $\mu_{HF}(\mu_B/\text{Co})$ | $\mu_{eff}(\mu_B/\text{Co})$ | $n_c$ | $m(\mu_B/\text{Co})$ |
|---|---|---|---|---|
| 150°C | 0.24 | 1.66 | 48 | 3.16 |
| 250°C | 0.12 | 0.97 | 65 | 1.95 |
| 400°C | 0.031 | 1.40 | - | - |
| 600°C | 0.14 | 0.98 | 49 | 1.87 |
| 800°C | 0.18 | 1.27 | 50 | 2.44 |

**Table 7.1.** *The saturation magnetic moment $\mu_{HF}$ and the effective moment $\mu_{eff}$ for different annealing temperatures as obtained from M vs. H measurements. The cluster size $n_c$ and average atomic magnetic moment m are calculated according to a model proposed by Néel for anti-ferromagnetic nanoparticles.*

Since we found significant amounts of spinels in 15% Co doped samples we can not use a magnetic moment of 3 $\mu_B$ for Co to calculate the cluster size since many of the Co atoms are non-magnetic in this compound. Instead we make no assumptions of the magnetic moment of Co and only make the assumption that the extracted cluster sizes should be consistent when using the saturation magnetic moment or the effective magnetic moment in the calculation. We observe that the magnetic moment for the non-heat treated sample (150° C) gives a value which is very close to expected value for substituted $Co^{2+}$. For

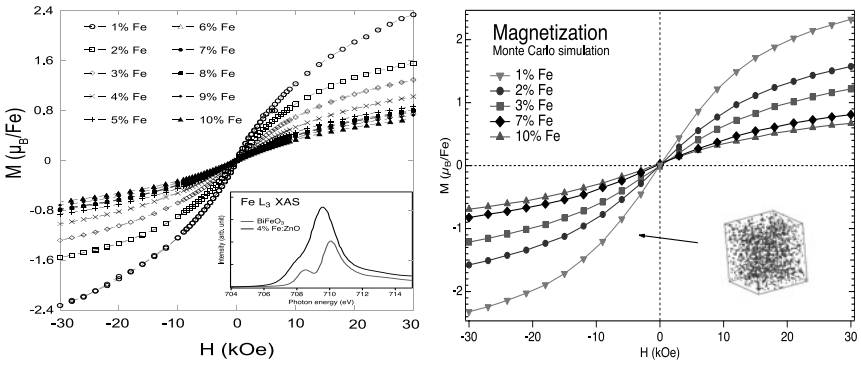


*Figure 7.9.* (left) Magnetization vs. field for 1 to 10% Fe doped ZnO. The inset shows the $Fe^{3+}$ character of the x-ray absorption spectra. (right) Monte Carlo simulations of Fe doped ZnO for different concentrations. The MCS and $J_{NN}$ is fixed to 9 and 0.2 mRy, respectively, for all concentrations.

the samples which are heat treated we observe a decrease of the magnetic moment as expected due to the presence of Co spinel. At 800° C the magnetic moment increases since the Co spinel is not stable at these temperatures.

Interestingly the cluster size is almost constant throughout the whole temperature range. This indicates that the clusters are created during the sample synthesis and are seemingly not affected by any heat treatment. We have not yet mentioned the 15% sample annealed at 400° C which clearly has a different behavior than the rest of the samples. This sample is saturated at very low fields and also have a much smaller saturation magnetic moment. The small value for the saturation field could suggest that this sample exhibits a long-range ferromagnetic order but this is difficult to reconcile with the small saturation magnetic moment. A more probable explanation is that spinels can exhibit a weak ferromagnetic behavior [45]. Both the saturation field and saturation magnetic moment of the ferromagnetic $ZnCo_2O_4$ corresponds well with the magnetization data obtained for the 400° C sample.

The magnetic properties of Fe doped ZnO has been analyzed in a different manner than for Co doping. In a similar way as clustering and percolation were studied theoretically by *ab initio* calculations and Monte Carlo simulations we made simulations for Fe doped ZnO. However, instead of calculating the chemical pair potential we made the assumption that the interaction between two nearest neighbor Fe atoms is strong enough to completely disable further diffusion in the ZnO lattice. We also made the assumption that all the Fe atoms have a 3+ oxidation state with a 5 $\mu_B$ magnetic moment. The number of Monte Carlo steps (MCS), which corresponds to the number of times every Fe atom can move in the lattice, and the nearest neighbor exchange interaction were used as parameters.

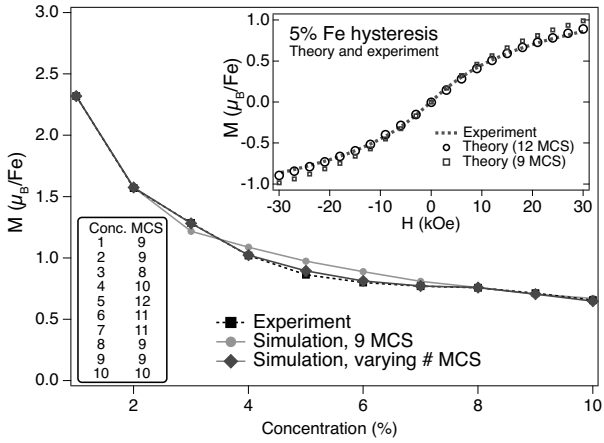


*Figure 7.10.* Experiment and simulation of the magnetization at 30 kOe. A constant MCS value of 9 gives a good fit to experimental results but it is improved by varying MCS for every sample. The box in the left corner gives the number of MCS used for the dopant concentrations. The inset shows experimental and simulated M vs. H data for the 5% sample.

The experimental magnetization versus field curve is shown in Fig. 7.9 (left) where the magnetization decreases with increasing doping concentration. A fit to the experimental data obtained from Monte Carlo simulations is shown in Fig. 7.9 (right), where we have used the same MCS (= 9) and nearest neighbor (NN) exchange interaction $J_{NN}$ (= -0.2 mRy) for all concentrations. Only the nearest neighbor exchange interaction has been taken into account and the negative value indicates that the interaction is anti-ferromagnetic. The correspondence between experiment and simulation can be improved by letting the number of MCS vary for different concentrations. We have plotted the experimental value of the magnetization at 30 kOe in Fig. 7.10 along with the simulation for both constant MCS and varying MCS. The box in the lower left corner shows the best fit MCS values for all concentrations. The inset in the upper right corner shows the experimental and simulated M vs. H curves for the 5% Fe doped sample. The agreement between experimental and simulated curves is excellent when using 12 MCS. For this sample almost all Fe atoms have at least one Fe NNs, while 50% of the atoms have 2 or 3 Fe NNs.

## 7.2 Interface investigation of multilayers

All the XPS experiments covered in this section were performed at the HIKE beamline KMC-1. The first two studies have in common that we are investigating chemical shifts in core-levels to study the intermixing between layers. For

the CFB/MgO we are using the large probing depth to investigate the diffusion and oxidation of boron in MgO tunnel barriers.

## CoMnGe/RhCuSn (Paper VIII)

The full-Heusler alloy is a ternary compound with the composition $X_2YZ$, where X and Y are two different transition metals and Z is a non-metal. $Co_2MnGe$ (CMG) is one of several magnetic Heusler alloys which have been proposed to be half-metallic. The Co based Heusler alloys are of special interest due to their high Curie temperatures which make them interesting for applications. Moreover, the potentially high spin polarization makes Heusler alloys very interesting for both TMR and current-perpendicular-to-plane (CPP) GMR structures [17, 43]. Some reported MR values in both types of structures are high but are typically difficult to realize in device fabrication [37, 55, 68, 77]. More generally the MR values are low, which is believed to come from disorder in the bulk and at interfaces, where the disorder is expected to be detrimental for the spin polarization [11, 66].

A CPP-GMR structure consisting of the non-magnetic Heusler $Rh_2CuSn$ (RCS) together with the magnetic CMG was claimed be less sensitive to bulk defects, low MR values (6.7%) was found also for this structure [1, 2, 58]. This GMR structure requires annealing at 250°C for setting the exchange bias, suggesting that it will be interesting to look for subtle change in the interface regions induced by heat treatment. We have investigated samples with different CMG and RCS layer thicknesses but the most studied sample is CMG(18 Å)/RCS(18 Å) denoted as "Thick layers". The CMG(18 Å)/RCS(6 Å) is denoted as "Thick magn. layer" and CMG(6 Å)/RCS(18 Å) is denoted "Thick non-magn. layer". If not stated otherwise, we always refer to the "Thick layers" sample.

In Fig. 7.11 (left) we present the Rh $3d_{5/2}$ core level after annealing to 265°C. All the data were collected with a photon energy of 4 keV. The Rh $3d_{5/2}$ was fitted with three main components and one weaker additional structure on the high BE side which decreased with increasing annealing temperature. The intensity of the main lines after heating the samples are presented on the right side of Fig. 7.11. The structure appears stable below 200°C but intensity is quickly transfered to the higher BE peaks when the temperature is increased above 200°C. We have also simulated diffusion by Monte Carlo simulations and counted the amount of Rh nearest neighbors for every Rh atom. The simulation illustrates well how the closest environment changes for the Rh atom as the sample is heated. The appearance of the low coordinated Rh peak before annealing suggests that the interface is not perfect.

The Mn $2p_{3/2}$ core level has been fitted by two components and presented in the left side of Fig. 7.12. The two components are referred to as the bulk and interface peaks. The bulk peak for the Thick magn. layer and Thick non-

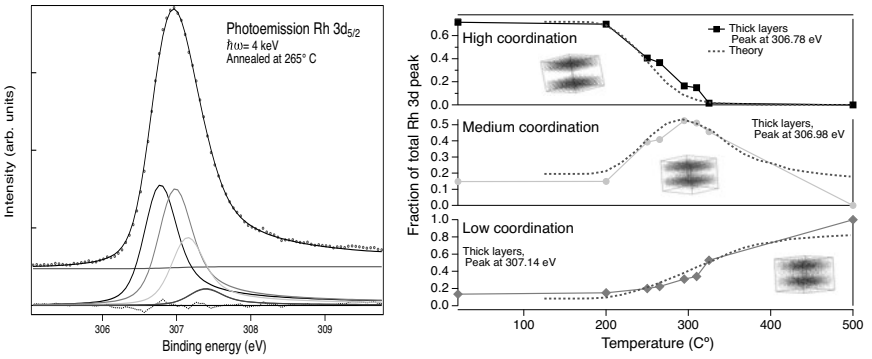


*Figure 7.11.* (left) Rh $3d_{5/2}$ core level fitted by four components after 265°C annealing. (right) The intensity of the three main peaks on the low BE side in the left figure are plotted as a function of temperature. Dashed red lines are Monte Carlo simulations of layer diffusion.

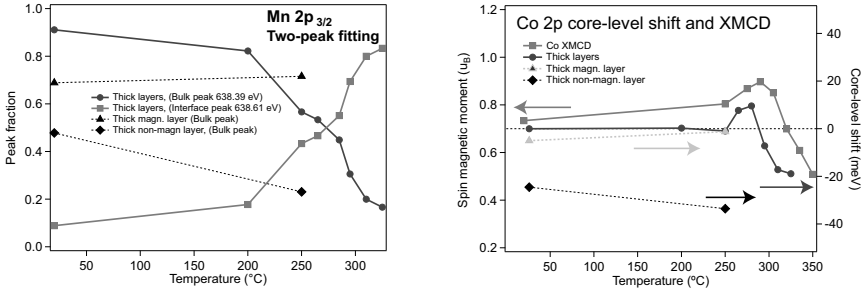


*Figure 7.12.* (left) Two peak fit of Mn $2p_{3/2}$ core level. The Mn seems to be sensitive to heat treatment above 200°C. (right) The core level shift of Co $2p_{3/2}$ (right axis) together with spin magnetic moment from XMCD (left axis). Both the magnetic moment and shift show an increase followed by a decrease in the same temperature region.

magn. layer samples are also shown for two temperatures. The Mn appears more mobile than Rh since a shift occurs already after 200°C. On the right side of Fig. 7.12 we show the chemical shift of Co $2p_{3/2}$ together with spin magnetic moments obtained with XMCD. Both the spin magnetic moment and the core level shift show an increase above 250°C after which they begin to decrease quickly around 280 - 300°C. The increase in magnetic moment can be due to Co atoms occupying Mn sites which supposedly increases the magnetic moment but is detrimental for the spin polarization [63, 58, 66].

We have observed that small changes in the multilayer structure occurs already at 200°C for some of the constituents. At 250°C large changes has occurred for many of the core levels, even though Co appears to be relatively stable. This could very well effect the efficiency of GMR structures which have been heat treated to 250°C.

## Cu/Ni (Papers IX, X)

Ni/Cu multilayer alloys are relatively easy to grow and the lattice mismatch is less than 3% [7]. The system is ideal for studying diffusion and we have here continued a previous study [31] to address the diffusion with a more careful and extended set of measurements. Magnetic properties of Ni/Cu has been studied as a model for ultra-thin film magnetism and in GMR structures [53, 57]. A set of Ni/Cu multilayer structures were grown on MgO(001) by magnetron sputtering. The samples differ both in the capping layer and the thickness of the Cu layer. They are referred to as $Ni_5Cu_5$/Pt, $Ni_5Cu_2$/Pt, and $Ni_5Cu_5$, where the thickness is given in monolayers. The non-Pt capped sample has a Ni cap which is carefully sputtered until the top oxide layer is removed.

The samples were annealed to study chemical shifts in Cu 2p, Ni 2p and Pt 4f core levels due to alloying. The Pt 4f showed only minor BE changes during the alloying process. We observe, in Fig. 7.13, that alloying is initiated already below 200°C and a large difference in chemical shift for Cu 2p is found between the Pt capped (left figure) and Ni capped (middle figure) samples. Using a photon energy of 2010 eV will give most of the intensity from the top two interfaces. This will not accurately describe the bulk intensities of the core-levels. We have therefore used a photon energy of 6030 eV in Fig. 7.13 (right) to increase the bulk sensitivity. These measurements are much more time consuming and hence the fewer data points. A large increase of the Cu/Ni intensity ratio (not shown) due to heating suggests that Cu segregates to the surface which explains the different behavior between the bulk (6030 eV) and more surface sensitive energy (2010 eV). *Ab initio* calculations for chemical shifts of Cu 2p were performed for disordered ternary alloys composed of NiCuPt for different concentrations of the three components shown in the left

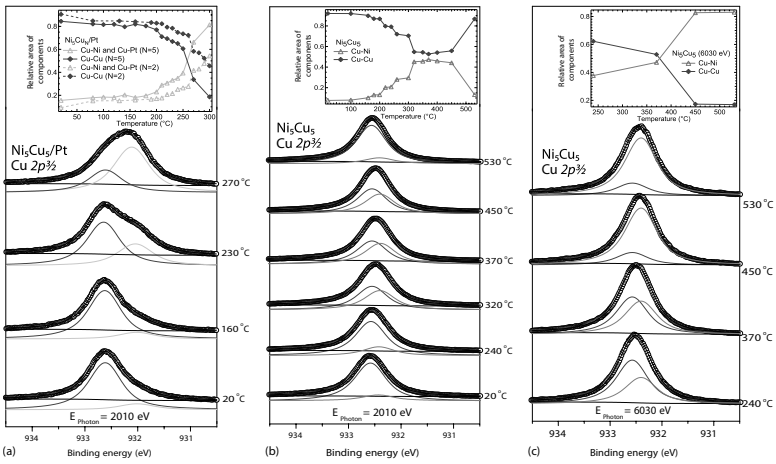


*Figure 7.13.* . A two peak-fit model of Cu $2p_{3/2}$ for sample $Ni_5Cu_5$ with and without Pt capping, (a) and (b) respectively, using 2010 eV photon energy. (c) The non-Pt capped sample using a more bulk sensitive photon energy of 6030 eV.

of Fig. 7.14. It is clear that the inclusion of Pt will increase the chemical shift as observed in Fig. 7.13.

The histograms in Fig. 7.14 are based on the intensity variations found in Fig. 7.13. We observe that already at 220°C there is an intermixing between Cu and Pt through the Ni layer.

## 7.3 Perpendicular magnetic anisotropy and boron diffusion in CoFeB/MgO (Paper VII)

Recently perpendicular magnetic anisotropy (PMA) was found in thin layered structures of CoFeB/MgO. The samples exhibited PMA only if the CoFeB (CFB) layer is close to 1 nm thick. Electric field switching of the perpendicular magnetization has been shown for CFB which is a property of high interest for spintronic applications. We have grown CFB/MgO bi-layers to study the magnetic properties of PMA-CFB using XMCD. The CFB was grown with different thicknesses, 0.8 nm, 1 nm, 1.2 nm and 3 nm respectively. A set of samples were annealed in 250°C with an out-of-plane (OP) field while one set remained non-annealed. The XMCD were performed in two geometries which are indicated on the right side of Fig. 7.16. First the incident x-rays were parallel with the surface normal where magnetization is 45° from the normal, see top right illustration of Fig. 7.16. The second geometry correspond to the bottom right illustration in Fig. 7.16, where the magnetizing field is close to in-plane.

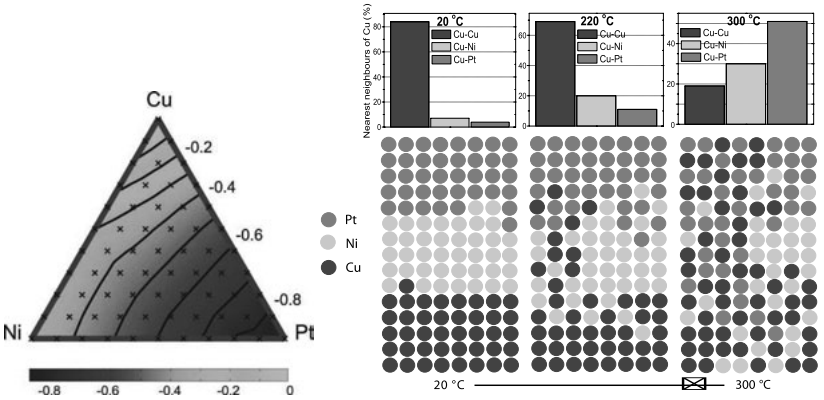


*Figure 7.14.* (left) Calculation of the chemical shift for Cu 2p in ternary NiCuPt disordered alloy. The three sides represents the concentration of each constituent. (right) An illustration of the alloying base on the intensities obtained from Fig. 7.13.

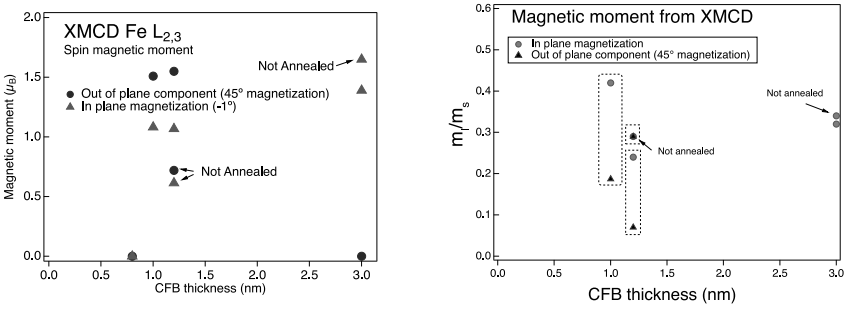


*Figure 7.15.* (left) The projected Fe spin magnetic moment for different CFB thicknesses. The thick 3 nm sample has no OP component, hence presented by its full moment i.e. not projected. (right) The ratio between orbital and spin magnetic moment. The dashed boxes surrounds each sample for clarity.

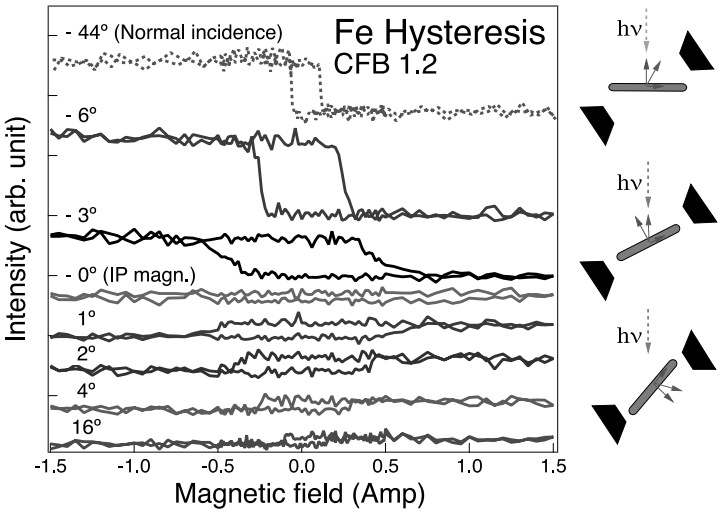


*Figure 7.16.* The Fe hysteresis for CFB 1.2 nm sample. The illustrations on the right side shows the geometry of the sample, incoming light and magnets for normal incidence and close to in-plane magnetization.

The projection of the spin magnetic moment parallel to the incident light is shown in Fig. 7.15 (left) except for the thick CFB 3 nm sample, which is presented as the total spin magnetic moment, since it only has an in-plane magnetization and therefore the remanent magnetization is well known. The non-annealed samples show a smaller spin moment for the CFB 1.2 nm while the thick CFB 3 nm sample shows a higher spin moment. The OP spin moment has very similar absolute value as the thicker CFB 3 nm sample. The orbital magnetic moment is presented in Fig. 7.15 (right) as the ratio between orbital- and spin- magnetic moments. The dashed boxes surrounds each sample for clarity and it is clear that the orbital magnetic moment is weaker in the OP direction. This is in contrast to what is usually found for PMA in fully metallic bi-layers where an increased OP orbital moment stabilizes the PMA. The Fe hysteresis was measured with partial fluorescence yield at different geometries as presented in Fig. 7.16 for sample CFB 1.2 nm. An interesting phenomena occurs close to in-plane magnetization where we observe a reversal of intensity on either side of in-plane geometry. This suggests that we are switching an OP component with an almost in-plane magnetic field. This assumption is strengthened by the increase of magnetic contrast for negative angles compared to positive as is shown in the lower two illustrations of Fig. 7.16 where the projected magnetic moment is larger for negative angles. The apparent increase of coersive field due to the decrease in OP magnetizing field is much smaller than would be anticipated.

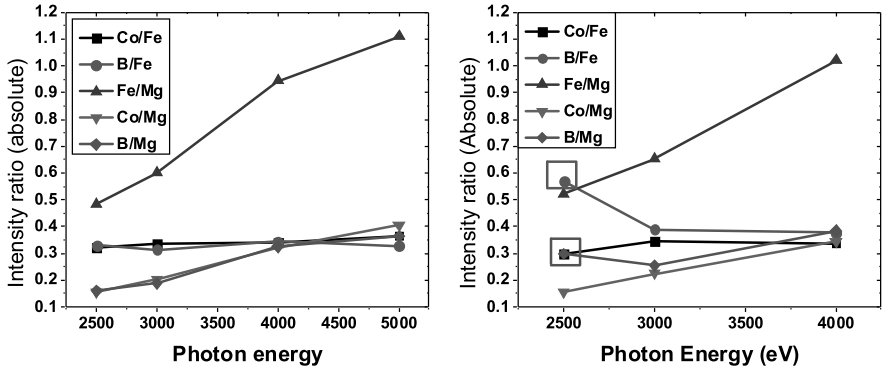


*Figure 7.17.* (left) The intensity ratio between different constituents in CFB/MgO. The Co, Fe and B are below the MgO, hence the intensity increase for increased photon energies. (right) After heating to 300°C the boron diffuses into MgO, increasing the B/Mg and B/Fe ratios.

We have also investigated boron diffusion into the MgO layer using HIKE. These measurements were done on two samples geometries, Ta(5)/CFB(5)/-MgO(2) and Ta(5)/CFB(5)/MgO(2)/CFB(1)/Ta(5), where the thickness is in nm and they will be denoted Ta-capped and non-capped, respectively. It is generally believed that boron is highly mobile and will diffuse into the MgO layer, forming boron oxide. We demonstrate that this is true only under certain conditions. The samples were measured with several photon energies and in Fig. 7.17 we have plotted the intensity ratio of different constituents for the non-capped sample. The intensity of Co, Fe and B increases compared to Mg with higher photon energies due to deeper probing depth (left Fig. 7.17). After annealing to 300°C there is a large increase for B at low energies (right Fig. 7.17), also a strong oxidation is observed for B, which are clear signs for boron diffusion. The Ta-capped sample shows a much more stable structure.

## 7.4 Magnetic anisotropy in MnAs/GaAs(100) (Paper VI)

The FM metal MnAs is interesting for spintronic applications since it can be grown on semiconductors such as Si and GaAs. Bulk MnAs has a first order phase transition at 313 K, where the FM hexagonal $\alpha$-phase goes into a orthorhombic $\beta$-phase [29]. The magnetic state of the $\beta$-phase was initially believed to be paramagnetic but later research indicates an AFM order [84, 50]. The transition temperature can be altered by structural strain and it has been shown that both the $\alpha$- and $\beta$-phases can co-exist close to $T_C$ [16, 67]. The tensile or compressive strain due to the substrate is known to have substantial effects on the magnetic properties of MnAs [52]. Also, the film growth is very

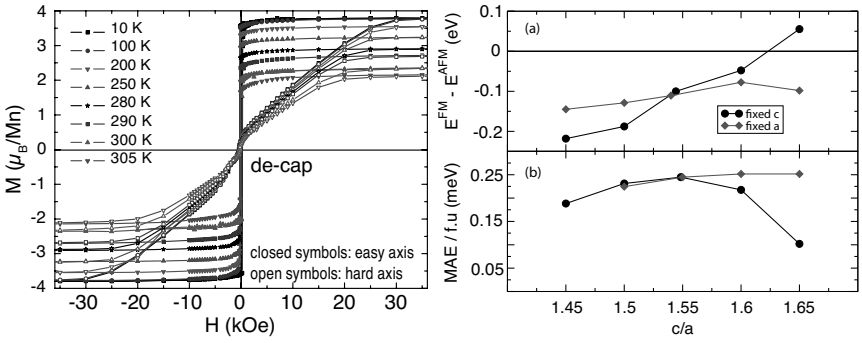


*Figure 7.18.* (Left) Magnetization (M) versus field (H) at different temperatures. The closed and open symbols corresponds to an applied field along the hard and easy axis respectively. (Right) (top) The energy difference between FM and AFM alignment of Mn spins. (bottom) The magnetic anisotropy energy (MAE) is sensitive to strain in the a-axis while its almost constant for c-axis strain.

sensitive to the surface reconstruction of the GaAs substrate. We have grown MnAs on different surface reconstructions of GaAs(001) by MBE. The study is focused on the dependence of magnetocrystalline anisotropy on strain which is studied both by experiment and theory. The c-axis, which is the magnetic hard axis, of MnAs grows in different directions depending on the growth conditions and especially on the surface reconstruction. A c(4x4) reconstruction on GaAs resulted in a film growth with the c-axis tilted mainly 29° out-of-plane, while the d(4x4) reconstruction yielded a film growth with the c-axis direction mainly in-plane.

SQUID magnetometry with the applied field along both the easy and hard magnetization direction, see Fig. 7.18, provides information of the anisotropy constants $K_1$ and $K_2$ at different temperatures. The derived value of $K_1$ for the d(4x4) samples are very close to the value obtained from *ab initio* calculations of the magnetic anisotropy energy (MAE), see Fig. 7.18, with values of $14 \times 10^5$ and 0.25 meV/f.u. $\approx 12 \times 10^5$ J/m$^3$ respectively.

XMCD was performed for a d(4x4) sample which showed an interesting temperature behavior close to the transition temperature. The derived spin and orbital magnetic moments as a function of temperature are presented in Fig. 7.19 (left). The measurements were performed in remanence after pulsing with a saturating magnetic field. The spin magnetic moment (a) has a similar temperature dependence as found by SQUID magnetometry but the orbital moment (b) shows an increase above 270 K. By comparing to the selected area electron diffraction (SAED) results (right) we observe that the $m_l/m_s$ ratio follows the same temperature dependence trend as the c/a ratio. A dependence

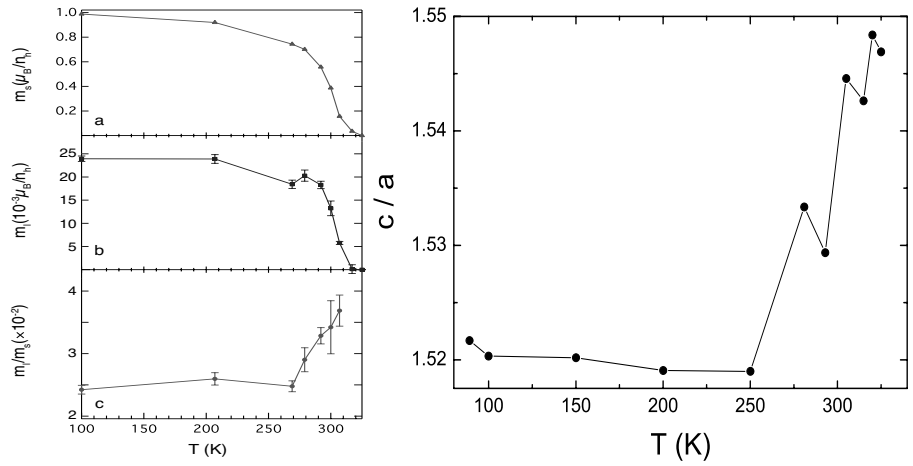


*Figure 7.19.* **a)**(left) Spin magnetic moment ($m_s$), **b)** orbital magnetic moment ($m_l$) and **c)** the ratio $m_l/m_s$. (right) Temperature dependence of the c/a ratio from SAED.

of the orbital magnetic moment on c/a ratio has been obtained by *ab initio* calculations. It is in this temperature range, 270-320 K, where we expect coexistence of the $\alpha$- and $\beta$-phases which induces a strain on the FM $\alpha$-phase domains.

## 7.5 Time resolved XMCD studies (Paper XI)

By using ferromagnetic resonance together with circularly polarized x-rays it is possible to study the precession of magnetic moment with elemental specificity. The pump-probe setup uses microwave magnetic excitation field which forces the magnetic moments into an harmonic motion when a bias field is applied. The microwave excitation is phase-locked to circularly polarized photon bunches used as the probe.

We have studied a trilayer consisting of two magnetic layers separated by a non magnetic layer, FeNi(15 nm)/Cu(10 nm)/CoZr(4 nm)/Cu(2 nm). The layers were deposited on a 100 nm thick silicon nitride membrane which allows the experiment to be performed in transmission mode. The intensity of the transmitted x-rays for different bias field is shown in Fig. 7.20 (a), where the bias field at resonance increases for increased microwave excitation frequencies, as expected for conventional FMR measurements. By applying a delay between pump and probe we can map the magnetization component along the direction of the transmitted x-rays at a function of time delay, shown in Fig. 7.20 (b). The signal contrast is diminished at higher frequencies primarily because of two factors: (i) the bunch width of the incoming photon probe, and (ii) the timing jitter of the probe with respect to the driving signal. However, a

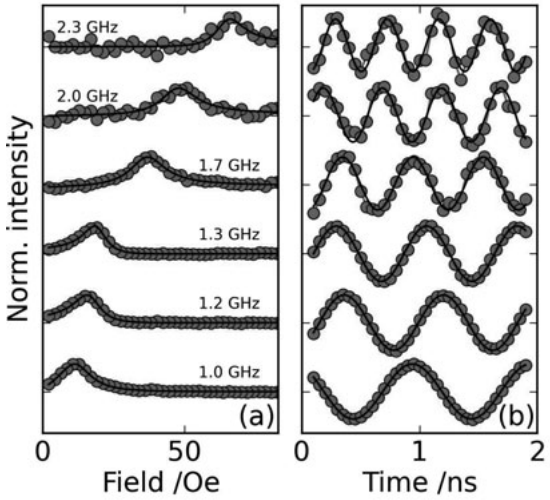


*Figure 7.20.* **a)** Normalized field scan at the $Fe_3$ edge. **b)** Time delay scans at the resonant field.

measurable contrast is still obtained using 2.5 GHz. This frequency is higher than expected for the bunch width of 650 ps (FWHM) delivered by the MAX-II synchrotron. Considering the bunch width of < 80 ps delivered at several synchrotrons it is feasible to extend the frequency range in which these types of experiments are normally conducted.

## 7.6 Conclusions and outlook

X-ray spectroscopy have been employed for both oxides and metallic systems which has given valuable information of electronic structure, magnetic properties and interface quality. The results presented for Co and Fe doped ZnO are discouraging in relation to potential DMS properties. Early theoretical results suggested that this material might be an intrinsic ferromagnet at room temperature but more recent calculations suggests otherwise. There is a general consensus that clustering is very likely to occur and that it has a detrimental effect on the desired DMS properties.

High kinetic x-ray photoelectron spectroscopy is a relatively recent characterization method, which we have used for metallic systems to study diffusion in multilayers. This is an attractive technique since the probing depth is in the same order as the thickness which the studied materials would have in actual devices. The diffusion of the capping layer in Ni/Cu multilayers was found to be an important factor which should be considered in future studies. For $Co_2MnGe$/$Rh_2CuSn$ Heusler multilayers, a different composition of the magnetic layer or a slightly changed device fabrication procedure could have major

effects on the MR since a large mobility in many of the constituents was observed at 250° C, while the diffusion was low at 200° C. Overall, Mn appears to be most mobile while Co is relatively stable. Large MR values of 70% has been found for CPP-GMR structures using a FM Heusler alloy with a transition metal spacer, which shows potential for future Heusler based CPP-GMR devices.

TMR devices composed of CoFeB/MgO with in-plane magnetic anisotropy has been used for several years as magnetic field sensor in hard drives. Recently a perpendicular magnetic anisotropy was found for ultra-thin CoFeB layers which has induced new research for this compound [35]. The PMA has shown to be manipulated by electric fields which opens up for new devices utilizing both the electric field sensitivity and PMA [76, 71]. Our studies show a large dependance on the orbital moment for in-plane and out-of-plane magnetization which is important information for accurate theoretical modeling of the observed PMA. However, non-annealed samples does not show this difference even though they exhibit PMA. This suggest a more complicated model than a simple change in the orbital moment anisotropy creating the PMA. It has been suggested that charge transfer in the CoFeB/MgO interface is responsible for the recently found PMA which could explain the sensitivity of PMA to electric fields. Time resolved XMCD studies has been performed on MgO substrates which would make CoFeB an interesting candidate to study.

# 8. Acknowledgement

Its been a crazy time which I have had the opportunity to experience the last few years. The solid state research begun with Biplab, with whom I did my masters thesis and the knowledge I got back then, I still have use for today. Thanks Biplab, Diana and Olle; also Patrik, Fredrik and Oscar my office mates back in the good old days.

I came into a completely different situation when Charlie thought that I should be his Ph.D student. No longer tied to a computer but kick out in the world, and even though we spent many nights and weekends inside synchrotron facilities it has been fun and I have, very much, enjoyed all the traveling. I want to thank Charlie for his support all these years and the chance to get experiences that will serve me my whole life, its been a pleasure. I have worked a lot with Peter and Magnus, great guys, and right now I feel very thankful for Peters, and Charlies, help to finish everything for this thesis. Also, Henrik "red beard", Biplab, Peter W has help with corrections. The work at synchrotrons would be impossible without the help from the experts Mats, Gunnar, Alexei, Nikolay, Ela and David. Perhaps the most important part for solid state research is good quality samples and for that I have Koroush, Gunnar, Victoria, Ulrika, Annika, Johan Å, Johan P, Ahn, and Janusz to thank for.

Davide and Andreas, my office mates which I have appriciated sharing my space with, much more fun than the big luxorious but lonely office I once had for myself, so no hard feelings Raimund. I want to thank Dario and Peter W for the time at long island and also Qin, Mark and Cecilia, I have had a great time there. My new friends from India, Anil, Debraj, Sumanta, Somnath, Sugata, Anindita, D.D. and everyone else I met in the land far far away, I'm really glad for the time over there. Matt for taking me to the next level in ping pong and good MAX-lab company which includes Pål as well. Thank you Rebecka and Andreas for the skrivar-pepp, as I said, it was needed. Josephina and Johan for making sure there is always lunch company in the corridor. The "guys" in the magnetism group who I always enjoy visiting Klas, Matthias, Per, Yajun and Rebecca. Everyone else that are/has been around me and making work enjoyable Wandared, Johan S, Martina, Atieh, Niklas, Nina, Svante, Nils, Paw, Carla, Rein, Stefan, Olle, Ruben, Dimitri, Sergei, Laurent, Anders, Håkan, Maria, Erik, Panos, Gabriella, Gunnar, Jan and probably many more if I had more time to think. Some of my friends, that creates life outside of work, should have credit, Hesso, Nicklas, Jonas K, Jonas L, Egil, Patrik och Malin, Uffe, maybe I will have time for fun stuff now again. Finally my greatest thanks to my family!

# References


[1] T. Ambrose and O. Mryasov. *Half-Metallic Alloys: Fundamentals and Applications, Lecture Notes in Physics*, volume Vol. 676. Springer, Berlin-New York, 2005.

[2] T. Ambrose and O. Mryasov. U.s. patent no. 6,876,522. Technical report, Seagate Inc., 2005.

[3] P. W. Anderson. Antiferromagnetism. theory of superexchange interaction. *Phys. Rev.*, 79:350–356, Jul 1950.

[4] P. W. Anderson. Ground state of a magnetic impurity in a metal. *Phys. Rev.*, 164(2):352, 1967.

[5] P. W. Anderson. Infrared catastrophe in fermi gases with local scattering potentials. *Phys. Rev. Lett.*, 18:1049–1051, Jun 1967.

[6] David Attwood. *Soft X-Rays and Extreme Ultraviolet Radiation: Principles and Applications*. Cambridge University Press, 2007.

[7] Harish C Barshilia and K.S Rajam. Characterization of cu/ni multilayer coatings by nanoindentation and atomic force microscopy. *Surface and Coatings Technology*, 155(2–3):195 – 202, 2002.

[8] L. Bergqvist, O. Eriksson, J. Kudrnovský, V. Drchal, P. Korzhavyi, and I. Turek. Magnetic percolation in diluted magnetic semiconductors. *Phys. Rev. Lett.*, 93:137202, Sep 2004.

[9] P. A. Brühwiler, O. Karis, and N. Mårtensson. Charge-transfer dynamics studied using resonant core spectroscopies. *Rev. Mod. Phys.*, 74(3):703, 2002.

[10] P. Bruno. Tight-binding approach to the orbital magnetic moment and magnetocrystalline anisotropy of transition-metal monolayers. *Phys. Rev. B*, 39:865–868, 1989.

[11] M.J. Carey et al. Band-structure calculations of imperfect Co2MnGe heusler compounds. *Appl. Phys. Lett.*, 85(19):4442 – 4, 2004.

[12] Paolo Carra, B. T. Thole, Massimo Altarelli, and Xindong Wang. X-ray circular dichroism and local magnetic fields. *Phys. Rev. Lett.*, 70(5):694, 1993.

[13] Sushin Chikazumi and Stanley H. Charap. *Physics of Magnetism*. Krieger Pub Co, 1978.

[14] T.J. Chuang, C.R. Brundle, and D.W. Rice. Interpretation of the x-ray photoemission spectra of cobalt oxides and cobalt oxide surfaces. *Surface Science*, 59(2):413 – 429, 1976.

[15] J. M. D. Coey. *Magnetism and Magnetic Materials*. Cambridge University Press, 2010.

[16] A. K. Das, C. Pampuch, A. Ney, T. Hesjedal, L. Däweritz, R. Koch, and K. H. Ploog. Ferromagnetism of MnAs studied by heteroepitaxial films on GaAs(001). *Phys. Rev. Lett.*, 91:087203, Aug 2003.

[17] R. A. de Groot, F. M. Mueller, P. G. van Engen, and K. H. J. Buschow. New class of materials: Half-metallic ferromagnets. *Phys. Rev. Lett.*, 50:2024–2027, Jun 1983.

[18] F. de Groth and Akio Kotani. *Core Level spectroscopy*. CRC Press, Taylor and Francis Group, New York, 2008.
[19] T. Dietl, H. Ohno, and F. Matsukura. Hole-mediated ferromagnetism in tetrahedrally coordinated semiconductors. *Phys. Rev. B*, 63(19):195205, 2001.
[20] T. Dietl, H. Ohno, F. Matsukura, J. Cibert, and D. Ferrand. Zener model description of ferromagnetism in Zinc-Blende magnetic semiconductors. *Science*, 287(5455):1019, 2000.
[21] Shuhua Dong, Kejing Xu, Juncheng Liu, and Hongwei Cui. Photocatalytic performance of ZnO:Fe array films under sunlight irradiation. *Physica B: Condensed Matter*, 406(19):3609 – 3612, 2011.
[22] Dongwoon and Jung. Syntheses and characterizations of transition metal-doped ZnO. *Solid State Sciences*, 12(4):466 – 470, 2010.
[23] F. Ducastelle. *Order and Phase Stability in Alloys*. North-Holland, Amsterdam, 1991.
[24] C. S. Fadley. *Electron Spectroscopy; Theory, Techniques and Applications*, volume 2. Academic Press, London, 1978.
[25] S. Gautam, S. Kumar, P. Thakur, K.H. Chae, R. Kumar, B.H. Koo, and C.G. Lee. Electronic structure studies of Fe-doped ZnO nanorods by x-ray absorption fine structure. *J. Phys. D: Appl. Phys.*, 42(17), 2009.
[26] M. Gorgoi, S. Svensson, F. Schäfers, G. Öhrwall, M. Mertin, P. Bressler, O. Karis, H. Siegbahn, A. Sandell, H. Rensmo, W. Doherty, C. Jung, W. Braun, and W. Eberhardt. The high kinetic energy photoelectron spectroscopy facility at bessy progress and first results. *Nucl. Instr. Meth. Phys. Res. A*, 601(1-2):48 – 53, 2009. Special issue in honour of Prof. Kai Siegbahn.
[27] Sari Granroth, Ronny Knut, Moreno Marcellini, Gabriella Andersson, Svante Svensson, Olof Karis, Mihaela Gorgoi, Franz Schäfers, Walter Braun, Wolfgang Eberhardt, Weine Olovsson, Erik Holmström, and Nils Mårtensson. Investigation of interface properties of Ni/Cu multilayers by high kinetic energy photoelectron spectroscopy. *Phys. Rev. B*, 80(9):094104, 2009.
[28] Helena A.E. Hagelin-Weaver, Gar B. Hoflund, David M. Minahan, and Ghaleb N. Salaita. Electron energy loss spectroscopic investigation of Co metal, CoO, and Co3O4 before and after ar+ bombardment. *Appl. Surf. Sci.*, 235(4):420 – 448, 2004.
[29] Siegfried Hilpert and Theodor Dieckmann. Über arsenide. i. (eisen- und manganarsenide.). *Berichte der Deutschen Chemischen Gesellschaft*, 44(3):2378–2385, 1911.
[30] P. Hohenberg and W. Kohn. Inhomogeneous electron gas. *Phys. Rev.*, 136:B864–B871, Nov 1964.
[31] E. Holmström, W. Olovsson, I. A. Abrikosov, A. M. N. Niklasson, B. Johansson, M. Gorgoi, O. Karis, S. Svensson, F. Schäfers, W. Braun, G. Öhrwall, G. Andersson, M. Marcellini, and W. Eberhardt. Sample preserving deep interface characterization technique. *Phys. Rev. Lett.*, 97:266106, Dec 2006.
[32] F. Holtzberg, S. von Molnar, and J. M. D. Coey. *Handbook on Semiconductors*, volume 3, page 850. Elsevier Science Ltd., 1980.
[33] http://www.maxlab.lu.se/beamlines/bld1011.
[34] S. Hüfner. *Photoelectron spectroscopy*. Springer-Verlag, Berlin Heidelberg

New York, 1995.
[35] S. Ikeda, K. Miura, H. Yamamoto, K. Mizunuma, H.D. Gan, M. Endo, S. Kanai, J. Hayakawa, F. Matsukura, and H. Ohno. A perpendicular-anisotropy CoFeB-MgO magnetic tunnel junction. *Nature Materials*, 9(9):721–724, 2010.
[36] D. Iuşan, M. Kabir, O. Grånäs, O. Eriksson, and B. Sanyal. Microscopic picture of Co clustering in ZnO. *Phys. Rev. B*, 79(12):125202, 2009.
[37] Taku Iwase, Yuya Sakuraba, Subrojati Bosu, Kesami Saito, Seiji Mitani, and Koki Takanashi. Large interface spin-asymmetry and magnetoresistance in fully epitaxial $Co_2MnSi$/Ag/$Co_2MnSi$ current-perpendicular-to-plane magnetoresistive devices. *Appl. Phys. Expr.*, 2(6):063003, 2009.
[38] E.M.J. Johansson, M. Odelius, M. Gorgoi, O. Karis, R. Ovsyannikov, F. Schafers, S. Svensson, H. Siegbahn, and H. Rensmo. Valence electronic structure of ruthenium based complexes probed by photoelectron spectroscopy at high kinetic energy (hike) and modeled by dft calculations. *Chem. Phys. Lett.*, 464(4-6):192 – 7, 2008.
[39] M. Julliere. Tunneling between ferromagnetic films. *Phys. Lett. A*, 54(3):225 – 226, 1975.
[40] T. Jungwirth, K. Y. Wang, J. Mašek, K. W. Edmonds, Jürgen König, Jairo Sinova, M. Polini, N. A. Goncharuk, A. H. MacDonald, M. Sawicki, A. W. Rushforth, R. P. Campion, L. X. Zhao, C. T. Foxon, and B. L. Gallagher. Prospects for high temperature ferromagnetism in (Ga,Mn)As semiconductors. *Phys. Rev. B*, 72(16):165204, 2005.
[41] O. Karis, S. Svensson, J. Rusz, P. M. Oppeneer, M. Gorgoi, F. Schafers, W. Braun, W. Eberhardt, and N. Martensson. High-kinetic-energy photoemission spectroscopy of ni at 1s: 6-ev satellite at 4 ev. *Phys. Rev. B*, 78(23):233105, 2008.
[42] T. Kataoka, M. Kobayashi, Y. Sakamoto, G.S. Song, A. Fujimori, F.-H. Chang, H.-J. Lin, D.J. Huang, C.T. Chen, T. Ohkochi, Y. Takeda, T. Okane, Y. Saitoh, H. Yamagami, A. Tanaka, S.K. Mandal, T.K. Nath, D. Karmakar, and I. Dasgupta. Electronic structure and magnetism of the diluted magnetic semiconductor Fe-doped ZnO nanoparticles. *J. Appl. Phys.*, 107(3):033718, 2010.
[43] M. I. Katsnelson et al. Half-metallic ferromagnets: From band structure to many-body effects. *Rev. Mod. Phys.*, 80(2):315–378, Apr 2008.
[44] A.D. Kent. Spintronics: Perpendicular all the way. *Nature Materials*, 9(9):699–700, 2010.
[45] Hyun Jung Kim, In Chang Song, Jae Ho Sim, Hyojin Kim, Dojin Kim, Young Eon Ihm, and Woong Kil Choo. Growth and characterization of spinel-type magnetic semiconductor $ZnCo_2O4$ by reactive magnetron sputtering. *Phys. Status Solidi B*, 241(7):1553, 2004.
[46] W. Kohn and L. J. Sham. Self-consistent equations including exchange and correlation effects. *Phys. Rev.*, 140:A1133–A1138, Nov 1965.
[47] R. Kumar, A.P. Singh, P. Thakur, K.H. Chae, W.K. Choi, B. Angadi, S.D. Kaushik, and S. Patnaik. Ferromagnetism and metal-semiconducting transition in Fe-doped ZnO thin films. *J. Phys. D: Appl. Phys.*, 41(15):155002, 2008.
[48] Q. H. Li, T. Gao, Y. G. Wang, and T. H. Wang. Adsorption and desorption of oxygen probed from ZnO nanowire films by photocurrent measurements. *Appl.*

*Phys. Lett.*, 86(12):123117, 2005.
[49] A. I. Liechtenstein, M. I. Katsnelson, V. P. Antropov, and V. A. Gubanov. Local spin density functional approach to the theory of exchange interactions in ferromagnetic metals and alloys. *J. Magnet. Magn. Mater.*, 67(1):65, 1987.
[50] J. Lindner, T. Toliński, K. Lenz, E. Kosubek, H. Wende, K. Baberschke, A. Ney, T. Hesjedal, C. Pampuch, R. Koch, L. Däweritz, and K.H. Ploog. Magnetic anisotropy of MnAs-films on GaAs(001) studied with ferromagnetic resonance. *J. Magnet. Magn. Mater.*, 277(1–2):159 – 164, 2004.
[51] G. D. Mahan. Collective excitations in x-ray spectra of metals. *Phys. Rev. B*, 11:4814–4824, Jun 1975.
[52] N. Menyuk, J. A. Kafalas, K. Dwight, and J. B. Goodenough. Effects of pressure on the magnetic properties of mnas. *Phys. Rev.*, 177:942–951, Jan 1969.
[53] T Mizuguchi, S Terada, T Miyauchi, and A Matsuzono. Characteristics of NiFe/CuNi multilayer GMR sensors for vertical GMR heads. *IEEE Trans. Magnetics*, 34:1504–1506, 1998.
[54] Peter Mohn. *Magnetism in the Solid State - An introduction*, volume 134 of *SPRINGER SERIES IN SOLID-STATE SCIENCES*. Springer, Berlin-New York, 2006.
[55] T. M. Nakatani, T. Furubayashi, S. Kasai, H. Sukegawa, Y. K. Takahashi, S. Mitani, and K. Hono. Bulk and interfacial scatterings in current-perpendicular-to-plane giant magnetoresistance with $Co_2Fe(Al_{0.5}Si_{0.5})$ heusler alloy layers and ag spacer. *Applied Physics Letters*, 96(21):212501, 2010.
[56] L. Néel. Superantiferromagnetisme dans les grains fins. *Compt. Rendu Hebd. Seances Acad. Sci.*, 252:4075, 1961.
[57] A. Ney, A. Scherz, P. Poulopoulos, K. Lenz, H. Wende, K. Baberschke, F. Wilhelm, and N. B. Brookes. Clarification of contesting results for the total magnetic moment of Ni/Cu(001). *Phys. Rev. B*, 65:024411, Dec 2001.
[58] K. Nikolaev, P. Kolbo, T. Pokhil, Xilin Peng, Yonghua Chen, T. Ambrose, and O. Mryasov. All-heusler alloy current-perpendicular-to-plane giant magnetoresistance. *Appl. Phys. Lett.*, 94(22):222501, 2009.
[59] P Nozières and C. T. De Dominicis. Singularities in the x-ray absorption and emission of metals. iii. one-body theory exact solution. *Phys. Rev.*, 178:1097, 1969.
[60] P. Nozières, J. Gavoret, and B. Roulet. Singularities in the x-ray absorption and emission of metals. ii. self-consistent treatment of divergences. *Phys. Rev.*, 178:1084, 1969.
[61] R. Nyholm, S. Svensson, J. Nordgren, and A. Flodström. A soft x-ray monochromator for the max synchrotron radiation facility. *Nucl. Instr. Meth. Phys. Res. A*, 246:267, 1986.
[62] Robert C. O'Handley. *Modern Magnetic Materials - Principles and Applications*. Wiley Interscience, 1999.
[63] S. Picozzi, A. Continenza, and A. J. Freeman. Role of structural defects on the half-metallic character of $co_2MnGe$ and $co_2MnSi$ heusler alloys. *Phys. Rev. B*, 69:094423, Mar 2004.
[64] G.A. Prinz. Magnetoelectronics applications. *J. Magn. Magn. Mater.*,

200(1-3):57, 1999.
[65] E. I. Rashba. Theory of electrical spin injection: Tunnel contacts as a solution of the conductivity mismatch problem. *Phys. Rev. B*, 62:R16267–R16270, Dec 2000.
[66] B. Ravel, J.O. Cross, M.P. Raphael, V.G. Harris, R. Ramesh, and V. Saraf. Atomic disorder in heusler Co2MnGe measured by anomalous x-ray diffraction. *Appl. Phys. Lett.*, 81(15):2812–2814, 2002.
[67] Kwang-Su Ryu, JinBae Kim, YoungPak Lee, Hiro Akinaga, Takashi Manago, Ravindranath Viswan, and Sung-Chul Shin. Origin of uniaxial magnetic anisotropy in epitaxial MnAs film on GaAs(001) substrate. *Applied Physics Letters*, 92(8):082503, 2008.
[68] Jo Sato, Mikihiko Oogane, Hiroshi Naganuma, and Yasuo Ando. Large magnetoresistance effect in epitaxial $Co_2Fe_{0.4}Mn_{0.6}Si$/Ag/$Co_2Fe_{0.4}Mn_{0.6}Si$ devices. *Applied Physics Express*, 4(11):113005, 2011.
[69] K. Sato, P.H. Dederichs, and H. Katayama-Yoshida. Local environment effects on exchange interactions in dilute magnetic semiconductors. *Phys. Status Solidi C*, 3(12):4143, 2006.
[70] G. Schmidt, D. Ferrand, L. W. Molenkamp, A. T. Filip, and B. J. van Wees. Fundamental obstacle for electrical spin injection from a ferromagnetic metal into a diffusive semiconductor. *Phys. Rev. B*, 62:R4790–R4793, Aug 2000.
[71] Y. Shiota, T. Nozaki, F. Bonell, S. Murakami, T. Shinjo, and Y. Suzuki. Induction of coherent magnetization switching in a few atomic layers of FeCo using voltage pulses. *Nature Materials*, 11(1):39–43, 2012.
[72] Joachim Stöhr. *NEXAFS Spectroscopy*. Springer-Verlag, Heidelberg, 1992.
[73] B. T. Thole, P. Carra, F. Sette, and G. van der Laan. X-ray circular dichroism as a probe of orbital magnetization. *Phys. Rev. Lett.*, 68(12):1943, 1992.
[74] G. Van der Laan and I.W. Kirkman. The 2p absorption spectra of 3d transition metal compounds in tetrahedral and octahedral symmetry. *J. Phys.: Condensed Matter*, 4(16):4189–4204, 1992.
[75] K. Y. Wang, R. P. Campion, K. W. Edmonds, M. Sawicki, T. Dietl, C. T. Foxon, and B. L. Gallagher. Magnetism in (Ga,Mn)As thin films with $T_C$ up to 173k. *AIP Conference Proceedings*, 772(1):333–334, 2005.
[76] Wei-Gang Wang, Mingen Li, Stephen Hageman, and C. L. Chien. Electric-field-assisted switching in magnetic tunnel junctions. *Nat Mater*, 11(1):64–68, 01 2012.
[77] Wenhong Wang, Enke Liu, Masaya Kodzuka, Hiroaki Sukegawa, Marec Wojcik, Eva Jedryka, G. H. Wu, Koichiro Inomata, Seiji Mitani, and Kazuhiro Hono. Coherent tunneling and giant tunneling magnetoresistance in Co2FeAl/MgO/CoFe magnetic tunneling junctions. *Phys. Rev. B*, 81:140402, Apr 2010.
[78] M. Weinelt, A. Nilsson, M. Magnuson, T. Wiell, N. Wassdahl, O. Karis, A. Föhlisch, , N. Mårtensson J. Stöhr, and M. Samant. Resonant photoemission at the 2p edges of ni: Resonant raman and interference effects. *Phys. Rev. Lett.*, 78:967, 1997.
[79] D. Weller, J. Stöhr, R. Nakajima, A. Carl, M. G. Samant, C. Chappert, R. Mégy, P. Beauvillain, P. Veillet, and G. A. Held. Microscopic origin of magnetic anisotropy in Au/Co/Au probed with x-ray magnetic circular dichroism. *Phys.*

*Rev. Lett.*, 75(20):3752, 1995.

[80] G.K. Wertheim and S. Hüfner. Many-body line shape in x-ray photoemission from metals. *Phys. Rev. Lett.*, 35:53, 1975.

[81] R.G. Wilks, E.Z. Kurmaev, J.C. Pivin, A. Hunt, M.V. Yablonskikh, D.A. Zatsepin, A. Moewes, S. Shin, P. Palade, and G. Principi. Ion irradiation induced reduction of Fe3+ to Fe2+ and Fe0 in triethoxysilane films. *J. Phys. Condens. Matter*, 17(43):7023–7028, 2005.

[82] S. A. Wolf, D. D. Awschalom, R. A. Buhrman, J. M. Daughton, S. von Molnár, M. L. Roukes, A. Y. Chtchelkanova, and D. M. Treger. Spintronics: A spin-based electronics vision for the future. *Science*, 294(5546):1488–1495, 2001.

[83] Qi Xiao and Chi Yao. Preparation and visible light photocatalytic activity of $Zn_{1-x}Fe_xO$ nanocrystalline. *Materials Chemistry and Physics*, 130(1-2):5 – 9, 2011.

[84] H Yamaguchi, AK Das, A Ney, T Hesjedal, C Pampuch, DM Schaadt, and R Koch. From ferro- to antiferromagnetism via exchange-striction of MnAs/GaAs(001). *Europhys. Lett.*, 72(3):479–485, 2005.

[85] C. Zener. Interaction between the d shells in the transition metals. *Phys. Rev.*, 81(3):440, 1951.

[86] Clarence Zener. Interaction between the d-shells in the transition metals. ii. ferromagnetic compounds of manganese with perovskite structure. *Phys. Rev.*, 82(3):403, 1951.

[87] H. Zhao, B. Glass, P.K. Amiri, A. Lyle, Y. Zhang, Y.-J. Chen, G. Rowlands, P. Upadhyaya, Z. Zeng, J.A. Katine, J. Langer, K. Galatsis, H. Jiang, K.L. Wang, I.N. Krivorotov, and J.-P. Wang. Sub-200ps spin transfer torque switching in in-plane magnetic tunnel junctions with interface perpendicular anisotropy. *J. Phys. D: Appl. Phys.*, 45(2), 2012.

Acta Universitatis Upsaliensis

*Digital Comprehensive Summaries of Uppsala Dissertations from the Faculty of Science and Technology* 897

Editor: The Dean of the Faculty of Science and Technology

A doctoral dissertation from the Faculty of Science and Technology, Uppsala University, is usually a summary of a number of papers. A few copies of the complete dissertation are kept at major Swedish research libraries, while the summary alone is distributed internationally through the series Digital Comprehensive Summaries of Uppsala Dissertations from the Faculty of Science and Technology.

Distribution: publications.uu.se
urn:nbn:se:uu:diva-167415

ACTA
UNIVERSITATIS
UPSALIENSIS
UPPSALA
2012